

# TIA1 Mutations in Amyotrophic Lateral Sclerosis and Frontotemporal Dementia Promote Phase Separation and Alter Stress Granule Dynamics

## Highlights

- Mutations affecting the low-complexity domain of TIA1 cause ALS and ALS-FTD
- ALS-linked *TIA1* mutations share a neuropathological TDP-43 signature
- *TIA1* mutations promote phase separation and impair stress granule dynamics
- TDP-43 recruited to poorly dynamic stress granules becomes immobile and insoluble

## Authors

Ian R. Mackenzie,  
Alexandra M. Nicholson,  
Mohona Sarkar, ..., Kevin B. Boylan,  
J. Paul Taylor, Rosa Rademakers

## Correspondence

jpaul.taylor@stjude.org (J.P.T.),  
rademakers.rosa@mayo.edu (R.R.)

## In Brief

Mackenzie et al. report the identification of mutations in *TIA1* as a novel cause of ALS and ALS-FTD. ALS-linked mutations perturb phase transitions of TIA1, which impair the dynamics of stress granules and indirectly promote TDP-43 insolubility.

# TIA1 Mutations in Amyotrophic Lateral Sclerosis and Frontotemporal Dementia Promote Phase Separation and Alter Stress Granule Dynamics

Ian R. Mackenzie,<sup>1,24</sup> Alexandra M. Nicholson,<sup>2,24</sup> Mohona Sarkar,<sup>3,24</sup> James Messing,<sup>3,23</sup> Maria D. Purice,<sup>3,23</sup> Cyril Pottier,<sup>2</sup> Kavya Annu,<sup>3</sup> Matt Baker,<sup>2</sup> Ralph B. Perkerson,<sup>2</sup> Aishe Kurti,<sup>2</sup> Billie J. Matchett,<sup>2</sup> Tanja Mittag,<sup>4</sup> Jamshid Temirov,<sup>3</sup> Ging-Yuek R. Hsiung,<sup>5</sup> Charles Krieger,<sup>5,6</sup> Melissa E. Murray,<sup>2</sup> Masato Kato,<sup>7</sup> John D. Fryer,<sup>2</sup> Leonard Petrucelli,<sup>2</sup> Lorne Zinman,<sup>8</sup> Sandra Weintraub,<sup>9</sup> Marsel Mesulam,<sup>9</sup> Julia Keith,<sup>8,10</sup> Sasha A. Zivkovic,<sup>11</sup> Veronica Hirsch-Reinshagen,<sup>1</sup> Raymond P. Roos,<sup>12</sup> Stephan Züchner,<sup>13</sup> Neill R. Graff-Radford,<sup>14</sup> Ronald C. Petersen,<sup>15</sup> Richard J. Caselli,<sup>16</sup> Zbigniew K. Wszolek,<sup>14</sup> Elizabeth Finger,<sup>17</sup> Carol Lippa,<sup>18,19</sup> David Lacomis,<sup>11,20</sup> Heather Stewart,<sup>5</sup> Dennis W. Dickson,<sup>2</sup> Hong Joo Kim,<sup>3</sup> Ekaterina Rogaeva,<sup>21</sup> Eileen Bigio,<sup>22</sup> Kevin B. Boylan,<sup>14</sup> J. Paul Taylor,<sup>3,23,25,\*</sup> and Rosa Rademakers<sup>2,\*</sup>

<sup>1</sup>Department of Pathology and Laboratory Medicine, Vancouver Coastal Health and the University of British Columbia, Vancouver, BC V6T 2B5, Canada

<sup>2</sup>Department of Neuroscience, Mayo Clinic Jacksonville, Jacksonville, FL 32224, USA

<sup>3</sup>Department of Cell and Molecular Biology

<sup>4</sup>Department of Structural Biology

St. Jude Children's Research Hospital, Memphis, TN 38105, USA

<sup>5</sup>Division of Neurology, Vancouver Coastal Health and the University of British Columbia, Vancouver, BC V6T 2B5, Canada

<sup>6</sup>Department of Biomedical Physiology and Kinesiology, Simon Fraser University, Burnaby, BC V5A 1S6, Canada

<sup>7</sup>Department of Biochemistry, University of Texas Southwestern Medical Center, Dallas, TX 75390, USA

<sup>8</sup>Sunnybrook Health Sciences Centre, Toronto, ON M4N 3M5, Canada

<sup>9</sup>Department of Neurology, Northwestern University Feinberg School of Medicine, Chicago, IL 60611, USA

<sup>10</sup>Department of Laboratory Medicine and Pathobiology, University of Toronto, Toronto, ON M5S 1A1, Canada

<sup>11</sup>Department of Neurology, University of Pittsburgh School of Medicine, Pittsburgh, PA 15213, USA

<sup>12</sup>Department of Neurology, University of Chicago Medicine, Chicago, IL 60637, USA

<sup>13</sup>Dr. John T. Macdonald Foundation, Department of Human Genetics and John P. Hussman Institute for Human Genomics, University of Miami Miller School of Medicine, Miami, FL 33136, USA

<sup>14</sup>Department of Neurology, Mayo Clinic Jacksonville, Jacksonville, FL 32224, USA

<sup>15</sup>Department of Neurology, Mayo Clinic Rochester, Rochester, MN 55905, USA

<sup>16</sup>Department of Neurology, Mayo Clinic Scottsdale, Phoenix, AZ 85054, USA

<sup>17</sup>Department of Clinical Neurological Sciences, Schulich School of Medicine and Dentistry, University of Western Ontario, London, ON N6A 5C1, Canada

<sup>18</sup>Department of Neurology, Drexel University College of Medicine, Philadelphia, PA 19107, USA

<sup>19</sup>Department of Neurology, Thomas Jefferson University, Philadelphia, PA 19107, USA

<sup>20</sup>Department of Pathology, University of Pittsburgh School of Medicine, Pittsburgh, PA 15213, USA

<sup>21</sup>Tanz Centre for Research in Neurodegenerative Diseases, University of Toronto, Toronto, ON M5T 2S8, Canada

<sup>22</sup>Department of Pathology, Northwestern University Feinberg School of Medicine, Chicago, IL 60611, USA

<sup>23</sup>Howard Hughes Medical Institute, Chevy Chase, MD 20815, USA

<sup>24</sup>These authors contributed equally

<sup>25</sup>Lead Contact

\*Correspondence: j.paul.taylor@stjude.org (J.P.T.), rademakers.rosa@mayo.edu (R.R.)

<http://dx.doi.org/10.1016/j.neuron.2017.07.025>

## SUMMARY

Amyotrophic lateral sclerosis (ALS) and frontotemporal dementia (FTD) are age-related neurodegenerative disorders with shared genetic etiologies and overlapping clinical and pathological features. Here we studied a novel ALS/FTD family and identified the P362L mutation in the low-complexity domain (LCD) of T cell-restricted intracellular antigen-1 (TIA1). Subsequent genetic association analyses showed an increased burden of *TIA1* LCD mutations in ALS patients compared to controls ( $p = 8.7 \times 10^{-6}$ ). Postmor-

tem neuropathology of five *TIA1* mutations carriers showed a consistent pathological signature with numerous round, hyaline, TAR DNA-binding protein 43 (TDP-43)-positive inclusions. *TIA1* mutations significantly increased the propensity of TIA1 protein to undergo phase transition. In live cells, *TIA1* mutations delayed stress granule (SG) disassembly and promoted the accumulation of non-dynamic SGs that harbored TDP-43. Moreover, TDP-43 in SGs became less mobile and insoluble. The identification of *TIA1* mutations in ALS/FTD reinforces the importance of RNA metabolism and SG dynamics in ALS/FTD pathogenesis.

## INTRODUCTION

Amyotrophic lateral sclerosis (ALS) is the most common motor neuron disease, characterized by progressive degeneration of upper and lower motor neurons that ultimately leads to death by respiratory failure (Taylor et al., 2016a). While most patients present with ALS alone, a subset of individuals present with concomitant frontotemporal dementia (ALS-FTD) (Hardy and Ro-  
gaeva, 2014). Recent gene discoveries and clinicopathological studies have highlighted that ALS and FTD are part of a disease continuum (ALS/FTD) with a shared genetic etiology (Ji et al., 2017; Neumann et al., 2006). Repeat expansions in the chromosome 9 open reading frame 72 gene (*C9orf72*) and mutations in *TBK1* (encoding TANK-binding kinase 1) and *TARDBP* (encoding transactive response DNA-binding protein 43, TDP-43) are among the most common genetic causes of the ALS-FTD phenotype, and notably, each of these mutations results in pathology characterized by TDP-43-positive neuronal cytoplasmic inclusions (Cirulli et al., 2015; DeJesus-Hernandez et al., 2011; Freischmidt et al., 2015; Kabashi et al., 2008; Renton et al., 2011; Sreedharan et al., 2008). However, the cause of a significant number of ALS and ALS-FTD cases remains unknown.

Many ALS-causing mutations impact proteins involved in RNA metabolism, including RNA-binding proteins such as TDP-43, fused in sarcoma (FUS), and heterogeneous nuclear ribonucleoprotein A1 (hnRNPA1) (Taylor et al., 2016a). These and related RNA-binding proteins are components of membrane-less organelles found in the nucleus (e.g., nuclear speckles and nucleoli) and cytoplasm (e.g., processing bodies and stress granules, SGs) of neurons and other cell types (Brangwynne et al., 2011; Collier et al., 1988; Huang and Spector, 1992; Sheth and Parker, 2003; Taylor et al., 2016b). It has recently emerged that biophysical properties encoded in prion-like, low-complexity sequence domains (LCDs) of RNA-binding proteins promote the assembly of membrane-less organelles through the process of liquid-liquid phase separation (LLPS) (Kato et al., 2012; Lin et al., 2015; Mollieix et al., 2015; Patel et al., 2015).

Here we report the identification of rare mutations impacting the LCD of the RNA-binding protein T cell-restricted intracellular antigen-1 (TIA1) in ALS and ALS-FTD patients. TIA1 is a prominent SG component and the LCD of TIA1 plays a central role in promoting SG assembly (Gilks et al., 2004; Kedersha et al., 2000; Panas et al., 2016). We found that disease-associated mutations alter biophysical properties of TIA1 by significantly increasing the propensity toward phase separation, delaying SG disassembly, and promoting the accumulation of non-dynamic SGs that harbor TDP-43. Moreover, TDP-43 recruited into SGs becomes less mobile and insoluble. These findings reinforce the importance of disturbed RNA metabolism in ALS/FTD and place altered membrane-less organelle dynamics at the center of ALS/FTD pathogenesis.

## RESULTS

### Identification of *TIA1* Mutations in Patients with ALS and ALS-FTD

We performed whole-exome sequencing in a pair of second-degree relatives with clinical features of both ALS and FTD

(ALS-FTD), and with autopsy-confirmed TDP-43 pathology. These individuals were from a multigenerational ALS/FTD family of European ancestry (UBCU2), negative for mutations in known ALS- and FTD-causing genes (Figure 1A). To identify candidate causal mutations, we filtered the genetic variants to those that were observed in the heterozygous state in both affected family members, altered the amino acid sequence, were absent from the Exome Variant Server population, and were present two or fewer times in the Exome Aggregation Consortium (ExAC) (Kobayashi et al., 2017). Among the 17 genes with such variants (all confirmed by Sanger sequencing), 15 were expressed in brain and five had variants with a combined annotation-dependent depletion (CADD) score >20, indicating that they are among the 1% most deleterious variants in the genome (Table S1). Interestingly, one of these was a missense variant (P362L) in *TIA1*. Similar to the ALS-related disease proteins TDP-43, hnRNPA1, and FUS, TIA1 is an RNA-binding protein containing a prion-like LCD and assembles into membrane-less organelles, including SGs (Taylor et al., 2016a). A different heterozygous founder mutation that affects the *TIA1* LCD (E384K) was previously reported in Swedish/Finnish patients as the cause of Welander distal myopathy (WDM) (Brand et al., 2016; Hackman et al., 2013; Klar et al., 2013), a rimmed vacuolar myopathy characterized by aggregates of TDP-43 and p62. WDM is clinically similar to and shares histopathological features with myopathies caused by mutations in valosin-containing protein (*VCP*), *p62/SQSTM1*, *HNRNPA1*, *HNRNPA2B1*, and *MATR3*, disease genes that have also been associated with ALS/FTD (Fecto et al., 2011; Johnson et al., 2010, 2014; Kim et al., 2013). Moreover, the P362L mutation in *TIA1* affects a highly conserved residue in the LCD (Figure 1B) and was predicted to be possibly damaging or deleterious by several in silico prediction algorithms (SIFT, PolyPhen, and Mutation Taster). Together, these observations led us to prioritize *TIA1* as an ALS/FTD candidate gene. To this end, we analyzed the *TIA1* LCD (encoded by exons 11–13) in a cohort of 1,039 ALS or ALS-FTD patients and 3,036 controls free of neurodegenerative diseases, and identified an increased burden of rare heterozygous *TIA1* mutations in patients compared to controls ( $p = 8.7 \times 10^{-6}$ , SKAT-O adjusted for age and sex). Specifically, in the association cohort we identified five additional *TIA1* mutations in a total of six unrelated patients, whereas no mutations were detected in controls (Figure 1B; Table S2). All *TIA1* mutations identified in patients had CADD scores >20 (Table S2).

### Clinical and Pathological Presentation of *TIA1* Mutation Carriers

The nine affected *TIA1* mutation carriers (three members of UBCU2 and six additional unrelated patients) had an average disease onset age of  $58.9 \pm 13.7$  years, with most patients presenting in mid-to-late adult life, with the exception of patient UBCU2-14, who had an unusually early onset of FTD and ALS symptoms at 28 years. Patients typically presented with either focal weakness or aphasia and all eventually developed ALS-type motor dysfunction, with accompanying features of FTD in five patients (Table S2). A positive family history of a similar neurodegenerative disease was documented in three of seven probands, resulting in a frequency of potential pathogenic *TIA1*

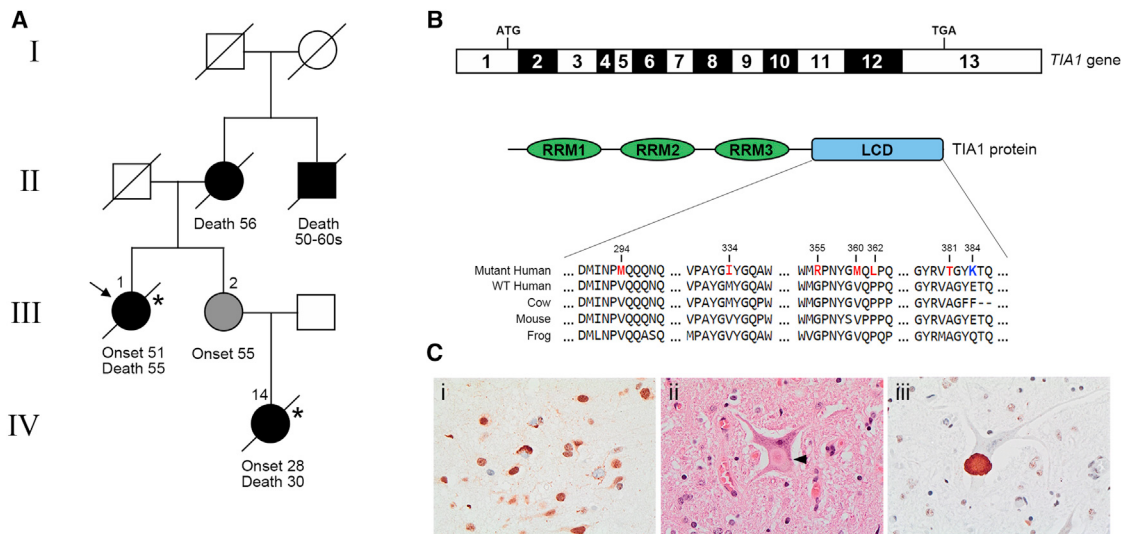


**Figure 1. *TIA1* Mutations Identified in Family UBCU2 and Patients with ALS or ALS-FTD**

(A) Abbreviated pedigree of the UBCU2 family of European ancestry included in this study showing unaffected individuals (white), individuals diagnosed with ALS or ALS-FTD (black), and an individual with early memory problems (gray). The proband is denoted with an arrow. Two family members with pathological diagnosis of ALS and FTLD-TDP were examined by whole-exome sequencing (\*). Sanger sequencing confirmed the *TIA1* P362L mutation in III-1, III-2, and IV-14, the only family members with DNA available.

(B) *TIA1* gene organization and protein structure with conserved regions of the TIA1 LCD. Mutations identified in this study are numbered and marked in red in relation to the known E384K mutation identified in Welander distal myopathy (blue).

(C) Images of autopsy pathology from patient UBCU2-1 showing TDP-43-immunoreactive neuronal cytoplasmic inclusions in the frontal cortex (i) and hyaline Lewy body-like cytoplasmic inclusions in lower motor neurons, demonstrated with hematoxylin and eosin stain (ii, arrowhead) and TDP-43 immunohistochemistry (iii).

See also Figure S1 and Tables S1–S3.

mutations in 2.2% of familial patients (3/136) and 0.4% of sporadic patients (4/903). Although all nine confirmed mutation carriers were female, there were affected males in some of the families. Autopsy material available for UBCU2-1, UBCU2-14, and three other unrelated patients (TOR-1, NWU-1, and ALS752-1) revealed TDP-43-immunoreactive pathology in the extra-motor neocortex (characteristic of FTLD-TDP type B), motor cortex, and spinal cord, which correlated with the clinical diagnoses of FTD and ALS in these patients, and which fell within the broad spectrum of pathology that is typically encountered in other cases of familial and sporadic ALS/FTD (Figures 1C and S1; Table S3). In addition, all five autopsy cases showed large, round, hyaline, Lewy body-like cytoplasmic inclusions in lower motor neurons, visible with hematoxylin and eosin staining (Figures 1Cii and S1) and also with TDP-43 immunohistochemistry (Figures 1Ciii and S1). Although similar hyaline Lewy body-like inclusions are occasionally seen in sporadic ALS patients, their frequency and consistent presence in the five *TIA1* mutation carriers suggest that these could be a pathological signature of *TIA1*-related disease (Figure S1). Immunohistochemistry and double-label immunofluorescence using a panel of commercial antibodies raised against different *TIA1* epitopes did not demonstrate any difference in staining between ALS/FTD patients with and without *TIA1* mutations; specifically, there was no co-localization of *TIA1* with TDP-43 immunoreactive inclusions (Figure S1). Consistent with these immunostaining results, protein extracts from postmortem tissue of *TIA1* mutation carriers did not show an obvious increase in *TIA1* levels in the urea fraction

as compared to protein extracts from non-*TIA1* mutation carriers and controls (Figure S1).

### Mutations Alter the Biophysical Properties of TIA1 to Promote LLPS

*TIA1* is a prototypical hnRNP that contains three RNA recognition motifs (RRMs) and a C-terminal LCD that is predicted to be intrinsically disordered (Figure 2A). LCDs in RNA-binding proteins such as hnRNPA1, TDP-43, and FUS contribute to the assembly of liquid-like membrane-less organelles such as SGs through the biophysical process of LLPS (Lin et al., 2015; Molliex et al., 2015; Murakami et al., 2015; Patel et al., 2015). Consistent with the behavior of these other RNA-binding proteins, the LCD (amino acids 290–386) of *TIA1* has been shown to undergo LLPS in the presence of RNA (Lin et al., 2015). We found that full-length *TIA1* spontaneously phase separated at room temperature, in the absence of any co-solute, at physiological ionic strength of 150 mM (pH 7.5) (Figures 2B, S2A, and S2B). To examine the impact of disease-associated mutations on LLPS of *TIA1*, we expressed and purified two ALS-associated *TIA1* mutants identified in this study (P362L and A381T) as well as the E384K mutant form associated with WDM (Figures 2A, S2A, and S2B) (Hackman et al., 2013; Klar et al., 2013). All three mutant proteins underwent spontaneous temperature- and concentration-dependent LLPS to create liquid droplets that at early time points were morphologically indistinguishable from liquid droplets formed by wild-type protein (Figure 2C). To quantify the propensity of each protein to undergo phase separation, we

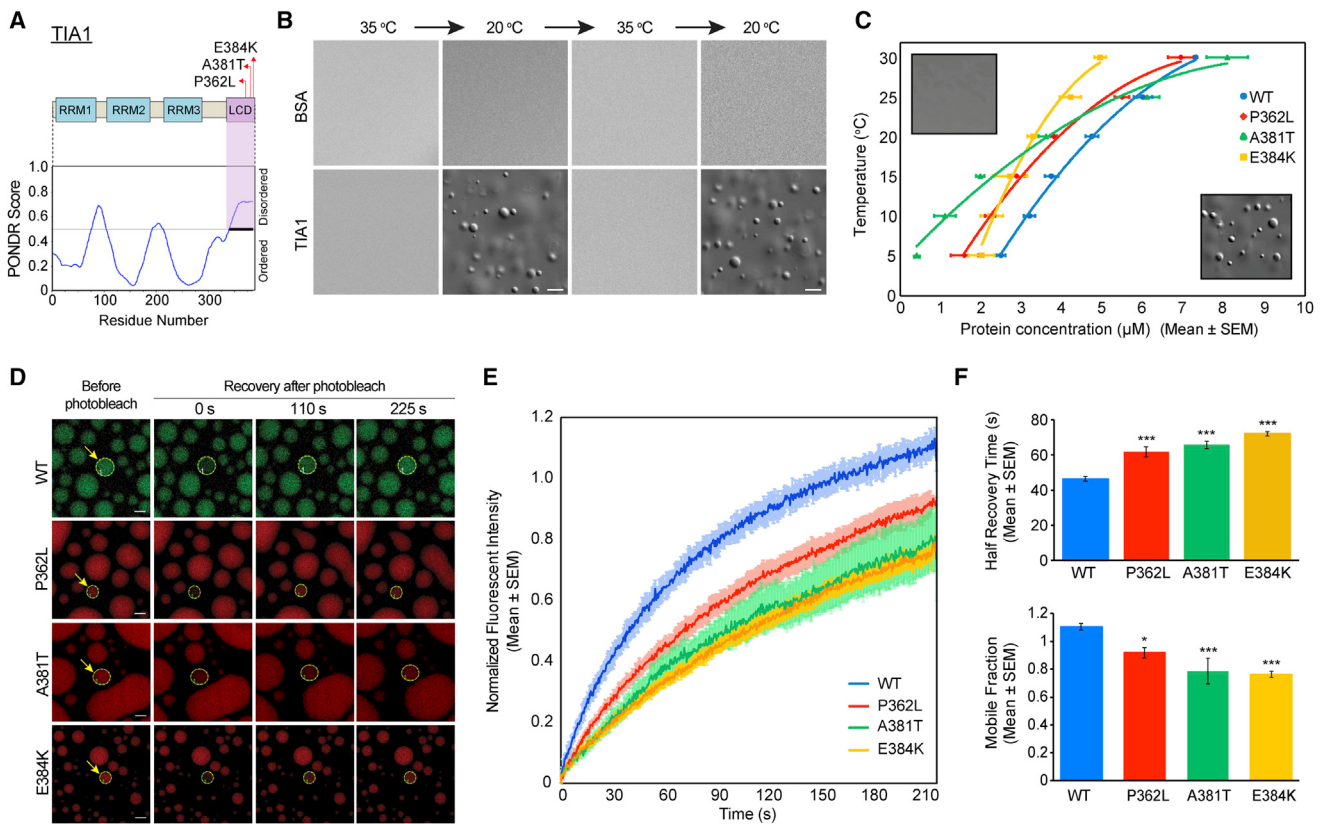


**Figure 2. Phase Separation and Mobility of TIA1 Are Altered by Disease-Causing Mutations**

(A) Schematic representation showing PONDR score along the length of wild-type TIA1, the location of the LCD, and the positions of disease-causing missense mutations P362L, A381T, and E384K.

(B) Temperature-sensitive, reversible phase separation of wild-type TIA1 was observed by DIC microscopy. BSA protein was used as a negative control.

(C) Phase diagrams (temperature [T] versus concentration) showing co-existence lines of wild-type, P362L, A381T, and E384K TIA1 (150 mM NaCl [pH 7.5] in absence of any co-solutes). Insets represent characteristic DIC images of single-phase (upper left) and two-phase (lower right) solutions of wild-type TIA1. n = 6 for wild-type and P362L, n = 3 for A381T and E384K; p < 0.001 for each variant compared to wild-type by Pearson's chi-square test.

(D) Disease-causing mutations P362L, A381T, and E384K reduce the mobility of TIA1 in the dense phase. Fluorescence images of wild-type or mutant TIA1 droplets 0–225 s after photobleaching within the region outlined in yellow (arrow).

(E) TIA1 fluorescence recovery after photobleaching in the dense phase indicates a significant reduction in mobility (n = 10 for E384K; n = 8 for P362L; n = 6 for wild-type and A381T). Recovery curves were normalized to background fluorescence (for subtracting noise) and adjacent non-bleached droplet (for fluorescence intensity fluctuations). p < 0.001 for each variant compared to wild-type by Pearson's chi-square test.

(F) Quantification of the half fluorescence recovery time and mobile fraction of wild-type and mutant TIA1. All graphs represent mean ± SEM. \*p < 0.05, \*\*\*p < 0.001 by one-way ANOVA with Dunnett's multiple comparisons test.

Scale bars, 20 (B) and 10 μm (D). See also Figure S2.

constructed a phase diagram by measuring the co-existence line of protein-depleted light phase and protein-enriched dense phase as a function of temperature and protein concentration. The P362L, A381T, and E384K mutant proteins caused a significant leftward shift in the co-existence line to a lower protein concentration, indicating an increased propensity of mutant TIA1 to phase separate, due to stronger intermolecular protein-protein interactions (Figure 2C).

Upon phase separation, the RNA-binding proteins hnRNPA1, FUS, and TDP-43 can access a spectrum of assemblies that exhibit progressively increased order and decreased mobility, ranging from liquid droplet to hydrogel to amyloid-like fibril (Schmidt and Görlich, 2016). Similar to observations in other RNA-binding proteins, we found that

when TIA1 droplets were allowed to settle on a coverslip surface and observed over time, droplets of mutant forms of TIA1 converted to thioflavin T (ThT)-positive fibrils within the liquid droplets within 45 min, at which time the droplets dissipated (Figure S2C). Although droplets of wild-type TIA1 also converted to ThT-positive fibrillary material followed by droplet dissolution, this process occurred over a much longer time course (i.e., ≥24 hr). Transmission electron micrographs confirmed the formation of amyloid-like fibrils of wild-type and mutant TIA1 (Figure S2D). Using a quantitative ThT fluorescence assay, we confirmed that disease-associated mutations in TIA1 significantly accelerated fibrillization of TIA1 (Figure S2E), similar to the consequence of disease-causing mutations in hnRNPA1, hnRNPA2B1, and FUS (Kim et al.,

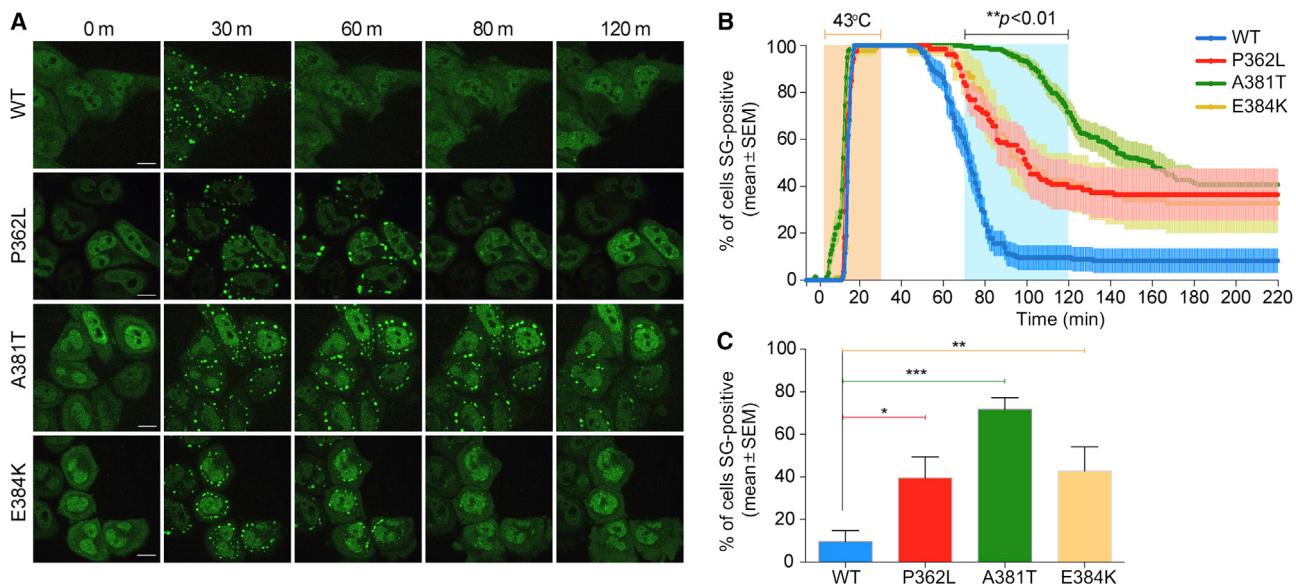


**Figure 3. Live-Cell Imaging Illustrates Prolongation of SG Recovery in Association with Disease-Causing TIA1 Mutations**

(A) Images of HeLa cells transfected with GFP-tagged wild-type or mutant (P362L, A381T, or E384K) TIA1. SGs were induced with a 30 min heat shock at 43°C (shaded in orange) and images were taken 0–120 min after recovery at 37°C.

(B) Line graph representing the percentage of cells with visible TIA1 puncta over time ( $n = 24, 8, 19$ , and  $8$  videos for wild-type, P362L, A381T, and E384K, respectively).

(C) Quantification of the percentage of cells with persistent SGs at 120 min. \* $p < 0.05$ , \*\* $p < 0.01$ , \*\*\* $p < 0.001$  by two-way ANOVA with Dunnett's multiple comparisons test. Scale bar, 10  $\mu$ m.

See also Figures S3 and S4 and Movie S1. All graphs represent the mean  $\pm$  SEM.

2013; Molliex et al., 2015; Patel et al., 2015). Although the importance of fibril formation in the normal physiological function of RNA-binding proteins and in disease pathogenesis is currently not known, these results provide further evidence that disease-associated mutations alter biophysical properties of TIA1; specifically, strengthening intermolecular interactions of TIA1 assemblies.

We next used fluorescence recovery after photobleaching (FRAP) to measure the mobility of fluorescently tagged TIA1 (Matsuda and Nagai, 2014). We found that disease-associated mutations significantly altered the dynamic exchange of TIA1 between the dense droplet phase and the light mono-disperse phase, with increased half-recovery times and a smaller overall mobile fraction (Figures 2D–2F). These results suggest that the mutations changed the material properties of mutant TIA1 droplets by enhancing transient, non-specific intermolecular interactions that reduce protein mobility. This observation raises the possibility that material properties of membrane-less organelles composed of TIA1 protein in live cells, such as SGs, could be adversely affected by the disease-associated mutations.

#### Mutations in TIA1 Impair Stress Granule Dynamics

TIA1 is a prominent SG component and the LCD of TIA1 plays a central role in promoting SG assembly (Gilks et al., 2004; Kedersha et al., 2000; Panas et al., 2016). To assess the impact of TIA1 mutations on SG dynamics, we established a live-cell assay that permits real-time monitoring of the kinetics of SG assembly and disassembly in response to a tightly controlled heat pulse. We

used this system to monitor SG dynamics in HeLa cells expressing N-terminal GFP-tagged TIA1 wild-type, P362L, A381T, or E384K mutants (Movie S1). GFP-tagged TIA1 showed the identical subcellular distribution as endogenous or untagged TIA1 proteins, and the frequency and size of SGs containing these proteins were not altered by introduction of exogenous TIA1 at this modest expression level (Figure S3). We observed no significant impact of the P362L, A381T, or E384K TIA1 mutations on the rates of SG assembly. By contrast, each of these disease-associated mutations resulted in significantly protracted SG disassembly, as assessed by both blinded manual counting and automated image analysis (Figures 3A, 3B, and S4A–S4D). The consequence of impaired SG disassembly in cells expressing mutant TIA1 was a significant accumulation of non-dynamic, TDP-43-containing SGs that persisted for hours after SGs had disappeared from the cells expressing wild-type TIA1 (Figures 3C and 4A). This finding is consistent with a prior report that the E384K WDM-causing mutation is associated with increased numbers of SGs that show dynamics alterations as assessed by FRAP (Hackman et al., 2013).

#### TDP-43 Recruited to Stress Granules Becomes Insoluble

TIA1 mutation carriers with ALS/FTD exhibit prominent TDP-43 pathology (Figures 1C and S1; Table S3). The impact of mutant TIA1 on SG dynamics and the abnormal accumulation of TDP-43-containing SGs prompted us to examine the relationship between SG dynamics and TDP-43 solubility. Upon stress, TDP-43 is recruited to TIA1-positive SGs (Figure 4A). To examine

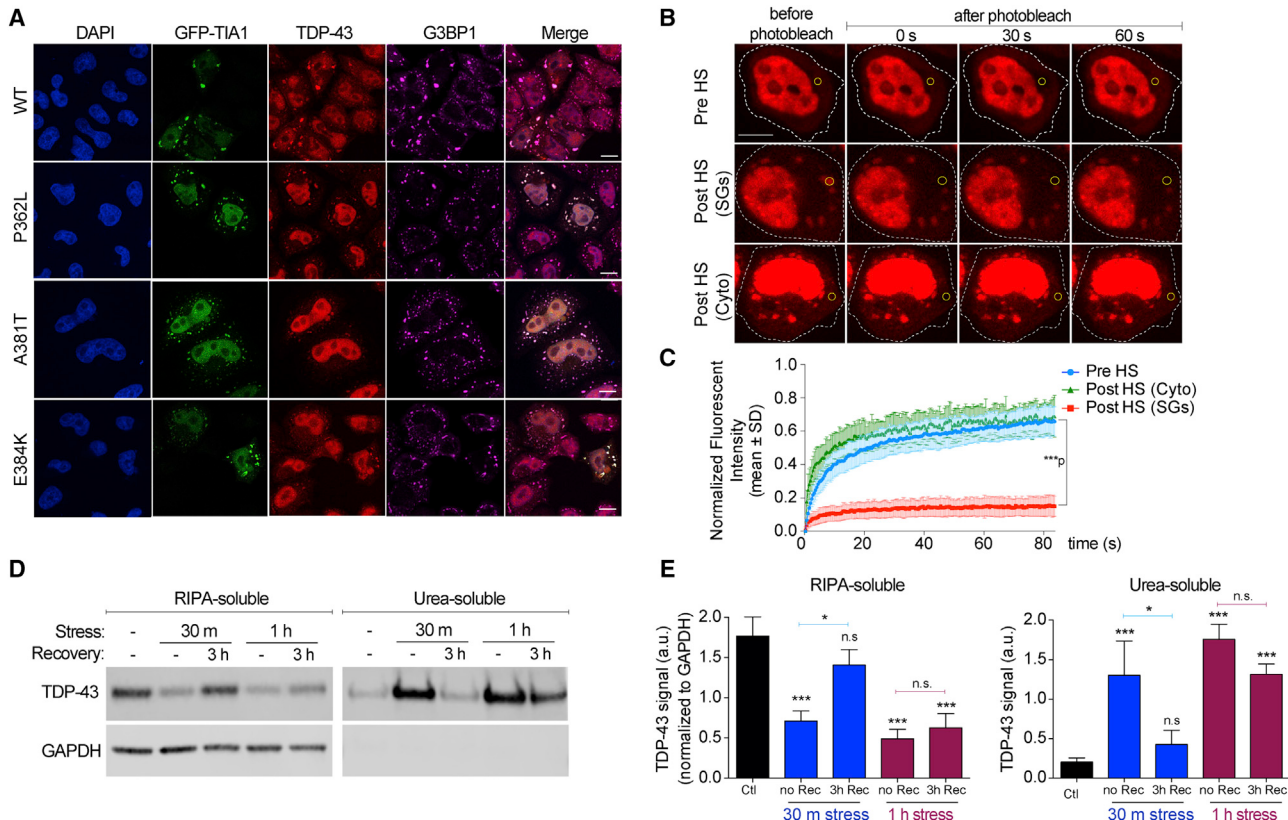


**Figure 4. TDP-43 Is Recruited to TIA1-Positive Stress Granules and TDP-43 Becomes Insoluble in Response to Stress**

(A) Immunofluorescence confocal microscopy shows intracellular co-localization of endogenous TDP-43 (using an antibody targeting the C terminus) with TIA1-positive stress granules of all four variants. GFP-tagged TIA1 constructs were transiently transfected in HeLa cells and cells were stressed with sodium arsenite for 30 min. Cells were fixed and stained with DAPI (blue), TDP-43 (red), and G3BP1 (far red), another marker of stress granules. Scale bar, 10  $\mu$ m.

(B) FRAP of TDP-43-TdTomato in HeLa cells (outlined in white) shows that cytoplasmic TDP-43 in resting cells (preHS, top row) is highly mobile. However, after heat shock stress, the TDP-43 that is recruited into SGs becomes immobile (middle row), while the TDP-43 that remains in the cytoplasm of the same cells (not in SGs, bottom row) remains highly mobile. Scale bar, 10  $\mu$ m.

(C) Quantification of FRAP analysis in (B). Pre-bleach, n = 15 cells; post-bleach, n = 16 cells (SGs) and 23 cells (cytoplasm). Graph represents the mean  $\pm$  SD.

(D) Prolonged sodium arsenite (Ars) stress promotes insolubility of TDP-43. Sequential extractions of U2OS cells under the following five conditions show that TDP-43 accumulates in the urea-soluble fraction in response to stress: (1) control (Ctl), (2) 30 min Ars, (3) 30 min Ars + 3 hr recovery (RE), (4) 1 hr Ars, and (5) 1 hr Ars + 3 hr RE.

(E) Quantification of RIPA and urea-soluble blots in (D) shows TDP-43 can recover from the urea-soluble to the RIPA-soluble fraction after a 30 min stress, but not after a 1 hr stress. n = 3 biological replicates. Graphs represent the mean  $\pm$  SEM. \*p < 0.05, \*\*\*p < 0.001 by one-way ANOVA with Dunnett's multiple comparisons test. n.s., not significant.

See also Figure S4.

the consequence of TDP-43 being recruitment into SGs, we transfected cells with TdTomato-tagged TDP-43 and assessed mobility of this protein using FRAP. In resting cells, TdTomato-TDP-43 in the nucleus and cytoplasm exhibited rapid mobility (Figures 4B and 4C). However, upon stress, the TdTomato-TDP-43 that was recruited to SGs became almost completely immobile, whereas the cytoplasmic TdTomato-TDP-43 that was not associated with SGs, in these same cells, remained mobile (Figures 4B and 4C). Biochemical assessment revealed a correlation between reduced mobility of TDP-43 upon recruitment to SGs and reduced TDP-43 solubility. Specifically, in resting cells TDP-43 was largely recovered in a detergent-soluble fraction (Figures 4D and 4E). In contrast, the TDP-43 derived from cells that had been stressed for 30 min showed a significant

shift from the detergent-soluble fraction to an insoluble pellet that was recovered by treatment with urea (Figures 4D and 4E). Notably, the solubility change that occurred under these conditions was reversible; 3 hr after recovery from the 30 min stress, and coincident with the clearance of SGs, TDP-43 returned to the detergent-soluble fraction (Figures 4D and 4E). However, the reversibility of insoluble TDP-43 accumulation was influenced by the duration of stress. Upon doubling the duration of stress from 30 min to 1 hr, we found that TDP-43 became permanently insoluble and failed to return to the detergent-soluble fraction after 3 hr of recovery. Taken together, these observations suggest that persistent, poorly dynamic SGs could promote the conversion of TDP-43 from a soluble to a stable insoluble form.

## DISCUSSION

Using exome sequencing in a novel ALS/FTD family, we identified the P362L mutation in the LCD of TIA1 as a strong causal candidate for disease. We subsequently identified five additional LCD *TIA1* mutations in a total of six unrelated patients, whereas none were found in controls free of neurodegenerative disease ( $p = 8.7 \times 10^{-6}$  in gene burden analysis). While the lack of mutations in our well-characterized control population suggests the *TIA1* mutations are causal ALS/FTD gene mutations (with an age-related disease penetrance), we acknowledge that the same *TIA1* mutations identified in our ALS/FTD patients are reported at very low frequency in the ExAC database (minor allele frequency  $< 0.0001$ ), classifying them as strong ALS/FTD risk factors instead. Using the European non-Finnish population from the ExAC database, an allele count of 26 is reported for rare *TIA1* alleles in the LCD, which, compared to the frequency in our ALS patients, would result in a conservative odds ratio (OR) of 6.9 (confidence interval, CI, 2.5–16.5) for *TIA1* allele carriers to develop ALS ( $p = 0.00018$ ). This is likely an underestimate that assumes that only 26,725 individuals in ExAC were sequenced for the entire gene, that all variants reported are real and observed in heterozygous state in independent individuals, and that all carriers would be free of ALS. This estimate also includes variants observed in ExAC with CADD  $\leq 20$ , whereas all mutations identified in our ALS patients had CADD  $> 20$ . The OR for carriers of a rare *TIA1* variant in the LCD with CADD  $> 20$  to develop ALS would be 15.1 (CI, 5.0–41.7;  $p = 3.4 \times 10^{-6}$ ). While future studies in ALS and FTD patient cohorts and control populations will be critical to evaluate the specific contribution of *TIA1* mutations to ALS/FTD, it is important to note that even the E384K mutation, considered pathogenic in WDM, is observed seven times in ExAC. Additionally, it is highly plausible that as-yet-unknown genetic and environmental factors affect the disease penetrance of *TIA1* mutations and that these factors may have contributed to the development of ALS/FTD in our patients. While speculative, the fact that all of our affected confirmed mutation carriers are females may suggest that these mutations are more penetrant in females than males; however, this also needs to be studied in additional cohorts. Importantly, detailed neuropathological analysis revealed strikingly uniform pathology with an unusually high frequency of hyaline Lewy body-like cytoplasmic inclusions in lower motor neurons in all five *TIA1* mutation carriers with autopsy confirmation (with four different *TIA1* mutations), further supporting a common pathomechanism in these patients. Overall, our findings suggest that *TIA1* mutations are a rare cause of ALS ± FTD, accounting for ~2% of familial ALS and <0.5% of sporadic ALS, frequencies that are comparable to those for mutations in other ALS genes such as VCP and profilin1 (*PFN1*) (Johnson et al., 2010; Wu et al., 2012).

Mounting evidence indicates that altered dynamics of membrane-less organelles such as SGs contribute to age-related degenerative diseases, including the most common forms of ALS, FTD, myopathy, and possibly Alzheimer's disease and other tauopathies (Aulas and Vande Velde, 2015; Brunello et al., 2016; Taylor et al., 2016a; Vanderweyde et al., 2012, 2016), although the precise molecular mechanism for this disturbance in some cases has been unclear. The LCDs of

RNA-binding proteins promote the assembly of membrane-less organelles through the process of LLPS (Lin et al., 2015; Molliex et al., 2015; Patel et al., 2015). Disease-causing mutations that impact the LCDs of several RNA-binding proteins, including hnRNPA1, FUS, and TDP-43, strengthen intermolecular LCD interactions, as evidenced by an increased propensity of these proteins to assemble into amyloid-like fibrils under experimental conditions (Kim et al., 2013; Molliex et al., 2015; Patel et al., 2015), although an impact on phase separation and the material properties of the liquid phase has not been previously documented and may be more physiologically relevant. Here we show that ALS/FTD-causing mutations in the LCD of the SG protein TIA1 significantly alter biophysical properties of the protein, strengthening its intermolecular interactions and enhancing its propensity to undergo phase transition. In cells, this perturbation of TIA1 results in poorly dynamic SGs that fail to appropriately disassemble and persist in the cytoplasm long after the removal of stress. We suggest that the accumulation of poorly dynamic SGs (and perhaps other membrane-less organelles that are composed of TIA1) creates an environment in which aggregation-prone molecules that are in high concentration (such as TDP-43) have an increased risk of gradually accumulating in an insoluble form (Neumann et al., 2006). Whereas TDP-43 forms detergent-resistant aggregates, TIA1 fibrils are labile and reversible; thus, it is uncertain whether one would expect TIA1 or related SG markers to persist as components of the fully mature TDP-43-positive inclusions that are present at the end stage of the human disease process. Although we found no evidence for such co-localization in post-mortem material from *TIA1* mutation carriers, prior studies have provided conflicting evidence as to whether or not TIA1 and other SG proteins co-localize with the TDP-43 pathology in cases of ALS and FTD in general (Aulas and Vande Velde, 2015). Importantly, the impact of ALS/FTD-associated *TIA1* mutations on SG dynamics mirrors the recent observation that toxic, arginine-containing poly-dipeptides produced by mutant *C9orf72* also disturb phase transitions mediated by LCDs and disturb the dynamics of membrane-less organelles, including SGs (Lee et al., 2016). This discovery adds to the increasing evidence of a common pathogenic mechanism among ALS, FTD, and myopathy caused by mutations in RNA-binding proteins related to disturbed dynamics of membrane-less organelles, and adds *TIA1* to the growing list of genes responsible for multisystem proteinopathies: a group of inherited pleiotropic degenerative disorders that can variably affect the nervous system, muscle, and bone (Taylor, 2015).

## STAR METHODS

Detailed methods are provided in the online version of this paper and include the following:

- KEY RESOURCES TABLE
- CONTACT FOR REAGENT AND RESOURCE SHARING
- EXPERIMENTAL MODEL AND SUBJECT DETAILS
  - Study Populations
  - Mammalian Cell Culture
  - Bacterial Cell Culture

## ● METHOD DETAILS

- Whole Exome Sequencing and Variant Calling
- Filtering of Variants
- Variant Confirmation and *TIA1* Screening
- Mutagenesis
- Immunofluorescence
- Live-Cell Time-Lapse Imaging and Fluorescence Recovery After Photobleaching
- Recombinant *TIA1* Cloning and Purification
- Phase Separation
- In Vitro Fibrillization
- Fluorescence Recovery After Photobleaching in Droplets
- Human Tissue Solubility Assay
- Cell Culture Solubility Assay
- Western Blotting
- Histology
- Immunohistochemistry (IHC)

## ● QUANTIFICATION AND STATISTICAL ANALYSIS

- Genetic Statistical Analyses
- Live-Cell Analysis
- Automated Image Analysis
- Phase Diagram, Fibrillization, and FRAP Analyses

## SUPPLEMENTAL INFORMATION

Supplemental Information includes four figures, three tables, and one movie and can be found with this article online at <http://dx.doi.org/10.1016/j.neuron.2017.07.025>.

## AUTHOR CONTRIBUTIONS

Sample collection, preparation, and clinical evaluation: I.R.M., M.B., G.-Y.R.H., C.K., L.Z., S.W., M.M., J.K., S.A.Z., N.R.G.-R., R.C.P., R.J.C., Z.K.W., R.P.R., D.W.D., E.F., C.L., D.L., H.S., E.R., E.B., and K.B.B. Performed experiments and data analysis: I.R.M., A.M.N., M.S., J.M., M.D.P., K.A., C.P., M.B., R.B.P., A.K., B.J.M., M.E.M., T.M., J.T., M.K., S.Z., V.H.-R., H.J.K., J.P.T., and R.R. Scientific planning and direction: I.R.M., A.M.N., M.S., J.M., C.P., J.D.F., L.P., H.J.K., J.P.T., and R.R. Manuscript preparation: I.R.M., A.M.N., M.S., J.M., M.D.P., C.P., H.J.K., J.P.T., and R.R.

## ACKNOWLEDGMENTS

This study used ALS samples from the NINDS Human Genetics Resource Center DNA and Cell Line Repository (<https://ccr.coriell.org/ninds>). This work was supported by the Mayo Clinic for Individualized Medicine, the Arizona Alzheimer's Consortium, the Howard Hughes Medical Institute (045104-Taylor), the Clinical Research in ALS and related disorders for Therapeutic Development (CReATE) Consortium (1U54NS092091), the Canadian Institutes for Health Research (74580), and NIH grants R35NS097974, R35NS097261, R35NS097273, P50AG016574, P50NS072187, P01NS084974, U01AG006576, U54NS092091, P30AG019610, R01AG031581, R01NS072248, and R01NS075764. This work was supported in part by the Canadian Consortium on Neurodegeneration in Aging (137794) and the ALS Canada-Brain Canada Hudson Grant. A.M.N. was supported by the Richard C. Kendall Fellowship and C.P. is supported by the Younkin Fellowship. The authors also thank Anderson Kanagaraj, Tammy M. Parsons, Nicole A. Finch, Nicole Milkovic, Mieu Brooks, Thomas Ravenscroft, Bruce Eckloff, Monica Castanedes-Casey, Virginia Phillips, Linda Rousseau, and Yingxue Ren for technical and bioinformatic assistance; Steve McKnight for access to transmission electron microscopy; and Regina-Maria Kolaitis for assistance with live-cell imaging. The authors also thank Natalia Nedelsky for manuscript editing and Ana M. Caputo, Pamela Desaro, Carla Palmucci, Amelia Robertson, Au-

drey Strongosky, Marife Fabros, and Pheth Sengdy for assistance with patient ascertainment.

Received: April 6, 2017  
Revised: May 27, 2017  
Accepted: July 24, 2017  
Published: August 16, 2017

## REFERENCES

- Aulas, A., and Vande Velde, C. (2015). Alterations in stress granule dynamics driven by TDP-43 and FUS: a link to pathological inclusions in ALS? *Front. Cell. Neurosci.* 9, 423.
- Brand, P., Dyck, P.J., Liu, J., Berini, S., Selcen, D., and Milone, M. (2016). Distal myopathy with coexisting heterozygous *TIA1* and *MYH7* Variants. *Neuromuscul. Disord.* 26, 511–515.
- Brangwynne, C.P., Mitchison, T.J., and Hyman, A.A. (2011). Active liquid-like behavior of nucleoli determines their size and shape in *Xenopus laevis* oocytes. *Proc. Natl. Acad. Sci. USA* 108, 4334–4339.
- Brunello, C.A., Yan, X., and Huttunen, H.J. (2016). Internalized Tau sensitizes cells to stress by promoting formation and stability of stress granules. *Sci. Rep.* 6, 30498.
- Cirulli, E.T., Lasseigne, B.N., Petrovski, S., Sapp, P.C., Dion, P.A., Leblond, C.S., Couthouis, J., Lu, Y.F., Wang, Q., Krueger, B.J., et al.; FALS Sequencing Consortium (2015). Exome sequencing in amyotrophic lateral sclerosis identifies risk genes and pathways. *Science* 347, 1436–1441.
- Collier, N.C., Heuser, J., Levy, M.A., and Schlesinger, M.J. (1988). Ultrastructural and biochemical analysis of the stress granule in chicken embryo fibroblasts. *J. Cell Biol.* 106, 1131–1139.
- DeJesus-Hernandez, M., Mackenzie, I.R., Boeve, B.F., Boxer, A.L., Baker, M., Rutherford, N.J., Nicholson, A.M., Finch, N.A., Flynn, H., Adamson, J., et al. (2011). Expanded GGGGCC hexanucleotide repeat in noncoding region of C9ORF72 causes chromosome 9p-linked FTD and ALS. *Neuron* 72, 245–256.
- Elbaum-Garfinkle, S., Kim, Y., Szczepaniak, K., Chen, C.C., Eckmann, C.R., Myong, S., and Brangwynne, C.P. (2015). The disordered P granule protein LAF-1 drives phase separation into droplets with tunable viscosity and dynamics. *Proc. Natl. Acad. Sci. USA* 112, 7189–7194.
- Fecto, F., Yan, J., Vemula, S.P., Liu, E., Yang, Y., Chen, W., Zheng, J.G., Shi, Y., Siddique, N., Arrat, H., et al. (2011). SQSTM1 mutations in familial and sporadic amyotrophic lateral sclerosis. *Arch. Neurol.* 68, 1440–1446.
- Freischmidt, A., Wieland, T., Richter, B., Ruf, W., Schaeffer, V., Müller, K., Marroquin, N., Nordin, F., Hübers, A., Weydt, P., et al. (2015). Haploinsufficiency of TBK1 causes familial ALS and fronto-temporal dementia. *Nat. Neurosci.* 18, 631–636.
- Gilks, N., Kedersha, N., Ayodele, M., Shen, L., Stoecklin, G., Dember, L.M., and Anderson, P. (2004). Stress granule assembly is mediated by prion-like aggregation of TIA-1. *Mol. Biol. Cell* 15, 5383–5398.
- Gonzalez, M., Falk, M.J., Gai, X., Postrel, R., Schüle, R., and Zuchner, S. (2015). Innovative genomic collaboration using the GENESIS (GEM.app) platform. *Hum. Mutat.* 36, 950–956.
- Hackman, P., Sarparanta, J., Lehtinen, S., Virola, A., Evilä, A., Jonson, P.H., Luque, H., Kere, J., Screen, M., Chinnery, P.F., et al. (2013). Welander distal myopathy is caused by a mutation in the RNA-binding protein TIA1. *Ann. Neurol.* 73, 500–509.
- Hardy, J., and Rogeava, E. (2014). Motor neuron disease and frontotemporal dementia: sometimes related, sometimes not. *Exp. Neurol.* 262 (Pt B), 75–83.
- Huang, S., and Spector, D.L. (1992). U1 and U2 small nuclear RNAs are present in nuclear speckles. *Proc. Natl. Acad. Sci. USA* 89, 305–308.
- Ji, A.L., Zhang, X., Chen, W.W., and Huang, W.J. (2017). Genetics insight into the amyotrophic lateral sclerosis/frontotemporal dementia spectrum. *J. Med. Genet.* 54, 145–154.

- Johnson, J.O., Mandrioli, J., Benatar, M., Abramzon, Y., Van Deerlin, V.M., Trojanowski, J.Q., Gibbs, J.R., Brunetti, M., Gronka, S., Wu, J., et al.; ITALSGEN Consortium (2010). Exome sequencing reveals VCP mutations as a cause of familial ALS. *Neuron* 68, 857–864.
- Johnson, J.O., Pioro, E.P., Boehringer, A., Chia, R., Feit, H., Renton, A.E., Pliner, H.A., Abramzon, Y., Marangi, G., Winborn, B.J., et al.; ITALSGEN (2014). Mutations in the Matrin 3 gene cause familial amyotrophic lateral sclerosis. *Nat. Neurosci.* 17, 664–666.
- Kabashi, E., Valdmanis, P.N., Dion, P., Spiegelman, D., McConkey, B.J., Vande Velde, C., Bouchard, J.P., Lacomblez, L., Pochigaeva, K., Salachas, F., et al. (2008). TARDBP mutations in individuals with sporadic and familial amyotrophic lateral sclerosis. *Nat. Genet.* 40, 572–574.
- Kato, M., Han, T.W., Xie, S., Shi, K., Du, X., Wu, L.C., Mirzaei, H., Goldsmith, E.J., Longgood, J., Pei, J., et al. (2012). Cell-free formation of RNA granules: low complexity sequence domains form dynamic fibers within hydrogels. *Cell* 149, 753–767.
- Kedersha, N., Cho, M.R., Li, W., Yacono, P.W., Chen, S., Gilks, N., Golan, D.E., and Anderson, P. (2000). Dynamic shuttling of TIA-1 accompanies the recruitment of mRNA to mammalian stress granules. *J. Cell Biol.* 151, 1257–1268.
- Kim, H.J., Kim, N.C., Wang, Y.D., Scarborough, E.A., Moore, J., Diaz, Z., MacLea, K.S., Freibaum, B., Li, S., Molliex, A., et al. (2013). Mutations in prion-like domains in hnRNPA2B1 and hnRNPA1 cause multisystem proteinopathy and ALS. *Nature* 495, 467–473.
- Klar, J., Sobol, M., Melberg, A., Mäbert, K., Ameur, A., Johansson, A.C., Feuk, L., Entesarian, M., Orlén, H., Casar-Borota, O., and Dahl, N. (2013). Welander distal myopathy caused by an ancient founder mutation in TIA1 associated with perturbed splicing. *Hum. Mutat.* 34, 572–577.
- Kobayashi, Y., Yang, S., Nykamp, K., Garcia, J., Lincoln, S.E., and Topper, S.E. (2017). Pathogenic variant burden in the ExAC database: an empirical approach to evaluating population data for clinical variant interpretation. *Genome Med.* 9, 13.
- Lee, K.H., Zhang, P., Kim, H.J., Mitrea, D.M., Sarkar, M., Freibaum, B.D., Cika, J., Coughlin, M., Messing, J., Molliex, A., et al. (2016). C9orf72 dipeptide repeats impair the assembly, dynamics, and function of membrane-less organelles. *Cell* 167, 774–788.e17.
- Lin, Y., Protter, D.S., Rosen, M.K., and Parker, R. (2015). Formation and maturation of phase-separated liquid droplets by RNA-binding proteins. *Mol. Cell* 60, 208–219.
- Matsuda, T., and Nagai, T. (2014). Quantitative measurement of intracellular protein dynamics using photobleaching or photoactivation of fluorescent proteins. *Microscopy (Oxf.)* 63, 403–408.
- Molliex, A., Temirov, J., Lee, J., Coughlin, M., Kanagaraj, A.P., Kim, H.J., Mittag, T., and Taylor, J.P. (2015). Phase separation by low complexity domains promotes stress granule assembly and drives pathological fibrillization. *Cell* 163, 123–133.
- Murakami, T., Qamar, S., Lin, J.Q., Schierle, G.S., Rees, E., Miyashita, A., Costa, A.R., Dodd, R.B., Chan, F.T., Michel, C.H., et al. (2015). ALS/FTD mutation-induced phase transition of FUS liquid droplets and reversible hydrogels into irreversible hydrogels impairs RNP granule function. *Neuron* 88, 678–690.
- Neumann, M., Sampathu, D.M., Kwong, L.K., Truax, A.C., Micsenyi, M.C., Chou, T.T., Bruce, J., Schuck, T., Grossman, M., Clark, C.M., et al. (2006). Ubiquitinlated TDP-43 in frontotemporal lobar degeneration and amyotrophic lateral sclerosis. *Science* 314, 130–133.
- Neumann, M., Kwong, L.K., Truax, A.C., Vanmassenhove, B., Kretzschmar, H.A., Van Deerlin, V.M., Clark, C.M., Grossman, M., Miller, B.L., Trojanowski, J.Q., and Lee, V.M. (2007). TDP-43-positive white matter pathology in frontotemporal lobar degeneration with ubiquitin-positive inclusions. *J. Neuropathol. Exp. Neurol.* 66, 177–183.
- Neumann, M., Kwong, L.K., Lee, E.B., Kremmer, E., Flatley, A., Xu, Y., Forman, M.S., Troost, D., Kretzschmar, H.A., Trojanowski, J.Q., and Lee, V.M. (2009). Phosphorylation of S409/410 of TDP-43 is a consistent feature in all sporadic and familial forms of TDP-43 proteinopathies. *Acta Neuropathol.* 117, 137–149.
- Panas, M.D., Ivanov, P., and Anderson, P. (2016). Mechanistic insights into mammalian stress granule dynamics. *J. Cell Biol.* 215, 313–323.
- Patel, A., Lee, H.O., Jawerth, L., Maharana, S., Jahnel, M., Hein, M.Y., Stoynov, S., Mahamid, J., Saha, S., Franzmann, T.M., et al. (2015). A liquid-to-solid phase transition of the ALS protein FUS accelerated by disease mutation. *Cell* 162, 1066–1077.
- Renton, A.E., Majounie, E., Waite, A., Simón-Sánchez, J., Rollinson, S., Gibbs, J.R., Schymick, J.C., Laaksovirta, H., van Swieten, J.C., Mallykangas, L., et al.; ITALSGEN Consortium (2011). A hexanucleotide repeat expansion in C9ORF72 is the cause of chromosome 9p21-linked ALS-FTD. *Neuron* 72, 257–268.
- Schmidt, H.B., and Görlich, D. (2016). Transport selectivity of nuclear pores, phase separation, and membraneless organelles. *Trends Biochem. Sci.* 41, 46–61.
- Sheth, U., and Parker, R. (2003). Decapping and decay of messenger RNA occur in cytoplasmic processing bodies. *Science* 300, 805–808.
- Sreedharan, J., Blair, I.P., Tripathi, V.B., Hu, X., Vance, C., Rogej, B., Ackerley, S., Durnall, J.C., Williams, K.L., Buratti, E., et al. (2008). TDP-43 mutations in familial and sporadic amyotrophic lateral sclerosis. *Science* 319, 1668–1672.
- Taylor, J.P. (2015). Multisystem proteinopathy: intersecting genetics in muscle, bone, and brain degeneration. *Neurology* 85, 658–660.
- Taylor, J.P., Brown, R.H., Jr., and Cleveland, D.W. (2016a). Decoding ALS: from genes to mechanism. *Nature* 539, 197–206.
- Taylor, N., Elbaum-Garfinkle, S., Vaidya, N., Zhang, H., Stone, H.A., and Brangwynne, C.P. (2016b). Biophysical characterization of organelle-based RNA/protein liquid phases using microfluidics. *Soft Matter* 12, 9142–9150.
- Vanderweyde, T., Yu, H., Varnum, M., Liu-Yesucevitz, L., Citro, A., Ikezu, T., Duff, K., and Wolozin, B. (2012). Contrasting pathology of the stress granule proteins TIA-1 and G3BP in tauopathies. *J. Neurosci.* 32, 8270–8283.
- Vanderweyde, T., Apicco, D.J., Youmans-Kidder, K., Ash, P.E., Cook, C., Lummertz da Rocha, E., Jansen-West, K., Frame, A.A., Citro, A., Leszyk, J.D., et al. (2016). Interaction of tau with the RNA-binding protein TIA1 regulates tau pathophysiology and toxicity. *Cell Rep.* 15, 1455–1466.
- Wang, K., Li, M., and Hakonarson, H. (2010). ANNOVAR: functional annotation of genetic variants from high-throughput sequencing data. *Nucleic Acids Res.* 38, e164.
- Wilkins, M.R., Gasteiger, E., Bairoch, A., Sanchez, J.C., Williams, K.L., Appel, R.D., and Hochstrasser, D.F. (1999). Protein identification and analysis tools in the ExPASy server. *Methods Mol. Biol.* 112, 531–552.
- Wu, M.C., Lee, S., Cai, T., Li, Y., Boehnke, M., and Lin, X. (2011). Rare-variant association testing for sequencing data with the sequence kernel association test. *Am. J. Hum. Genet.* 89, 82–93.
- Wu, C.H., Fallini, C., Ticozzi, N., Keagle, P.J., Sapp, P.C., Piotrowska, K., Lowe, P., Koppers, M., McKenna-Yasek, D., Baron, D.M., et al. (2012). Mutations in the profilin 1 gene cause familial amyotrophic lateral sclerosis. *Nature* 488, 499–503.
- Zhang, Y.J., Xu, Y.F., Dickey, C.A., Buratti, E., Baralle, F., Bailey, R., Pickering-Brown, S., Dickson, D., and Petruccielli, L. (2007). Progranulin mediates caspase-dependent cleavage of TAR DNA binding protein-43. *J. Neurosci.* 27, 10530–10534.

**STAR★METHODS****KEY RESOURCES TABLE**

REAGENT or RESOURCE	SOURCE	IDENTIFIER
<b>Antibodies</b>		
Mouse monoclonal $\alpha$ -alpha-Synuclein (clone LB509)	Thermo Fisher Scientific	Cat #180215; RRID: AB_86714
Mouse monoclonal $\alpha$ -beta-Amyloid (clone 6f/3D)	DAKO	Cat #M0872; RRID: AB_2056966
Goat polyclonal $\alpha$ -eIF3 $\eta$	Santa Cruz	Cat # sc-16377; RRID: AB_671941
Rabbit polyclonal $\alpha$ -FUS	Sigma-Aldrich	Cat #HPA008784; RRID: AB_1849181
Mouse monoclonal $\alpha$ -G3BP	BD Biosciences	Cat #611127; RRID: AB_398438
Mouse monoclonal $\alpha$ -p62	BD Biosciences	Cat #610832; RRID: AB_398151
Mouse monoclonal $\alpha$ -hyperphospho-Tau (Ser202/Thr205; clone AT8)	Innogenetics	Cat #MN1020; RRID: AB_223648
Rat monoclonal $\alpha$ -pTDP-43 (clone 1D3)	Gift from Dr. Manuela Neumann	Neumann et al., 2009
Rabbit polyclonal $\alpha$ -TDP-43	ProteinTech	Cat #10782-2-AP; RRID: AB_615042
Rabbit polyclonal $\alpha$ -TDP-43 (C-terminal)	ProteinTech	Cat #12892-1-AP; RRID: AB_2200505
Mouse monoclonal $\alpha$ -TIA1	Beckman Coulter	Cat #IM2550; RRID: AB_131704
Rabbit monoclonal $\alpha$ -TIA1	Abcam	Cat #ab140595
Rabbit polyclonal $\alpha$ -TIA1	Abcam	Cat #ab40693; RRID: AB_2201438
Rabbit polyclonal $\alpha$ -TIA1	ProteinTech	Cat #12133-2-AP; RRID: AB_2201427
Goat polyclonal $\alpha$ -TIA1 (clone C-20)	Santa Cruz	Cat #sc-1751; RRID: AB_2201433
Mouse monoclonal $\alpha$ -TIA1/TIAR (clone D-9)	Santa Cruz	Cat #sc-48371; RRID: AB_628358
Rabbit polyclonal $\alpha$ -TIA1/TIAR (clone H-120)	Santa Cruz	Cat #sc-28237; RRID: AB_2201430
Rabbit polyclonal $\alpha$ -Ubiquitin	DAKO	Cat #Z0458; RRID: AB_2315524
Mouse monoclonal $\alpha$ -GAPDH (clone 6C5)	Santa Cruz	Cat #32233; RRID: AB_627679
Alexa Fluor 488	Molecular Probes	Cat #A11055; RRID: AB_2534102
Alexa Fluor 555	Molecular Probes	Cat #A31572; RRID: AB_162543
Alexa Fluor 647	Molecular Probes	Cat #A31571; RRID: AB_162542
Biotinylated goat $\alpha$ -rat	Jackson Immunoresearch	Cat #112-065-167; RRID: AB_2338179
<b>Bacterial and Virus Strains</b>		
One Shot TOP10 chemically competent <i>E. coli</i>	Life Technologies	Cat #C404003
Hi-Control BL21(DE3) Chemically Competent Cells (SOLOS)	Lucigen Corporation	Cat #60435-1
<b>Biological Samples</b>		
75 DNA samples from ALS patients	Coriell Institute for Medical Research	N/A
<b>Chemicals, Peptides, and Recombinant Proteins</b>		
1X TrypLE Express	Thermo Fisher Scientific	Cat #12604-013
Aminoethylcarbazole	Roche Diagnostics	Cat #760-020
AMPure SPRI beads	Beckman Coulter Genomics	Cat #A63882
Ampure XP beads	Beckman Coulter Genomics	Cat #A63882
Big Dye Terminavor V3.1	Life Technologies	Cat #4337456
Dynabeads MyOne Streptavidin T1	Thermo Fisher Scientific	Cat #65601
EnVision+System-HRP for mouse primary antibodies	DAKO	Cat #K4007
EnVision+System-HRP for rabbit primary antibodies	DAKO	Cat #K4011

(Continued on next page)

***Continued***

REAGENT or RESOURCE	SOURCE	IDENTIFIER
FuGENE 6 transfection reagent	Promega	Cat #E2691
His-SUMO-TIA1 A381T	This study	N/A
His-SUMO-TIA1 E384K	This study	N/A
His-SUMO-TIA1 P362L	This study	N/A
His-SUMO-TIA1 wild-type	This study	N/A
Illumina HiSeq paired-end cluster kit version 3	Illumina	Cat #PE-401-3001
Novex Tris-Glycine SDS Sample Buffer	Life Technologies	Cat #LC2676
Oregon Green Protein Labeling Kit	Molecular Probes	Cat #O10241
ProLong Gold antifade reagent with DAPI	Life Technologies	Cat #P36931
QuickChange Site-Directed Mutagenesis Kit	Agilent	Cat #210516
Sodium Arsenite, 0.05M	Sigma-Aldrich	Cat #35000-1L-R
SureSelect XT Human Exome+UTR v5	Agilent	Cat #5190-6215
Texas Red Protein Labeling Kit	Molecular Probes	Cat # T10244
Thioflavin T (ThT)	Sigma-Aldrich	Cat #T3516
TrueSeq SBS sequencing kit version 3	Illumina	Cat #FC-401-3001
β-D-1-thiogalactopyranoside (IPTG)	Sigma-Aldrich	Cat #I5502
Experimental Models: Cell Lines		
HeLa cells	ATCC	Cat #CCL-2; RRID: CVCL_0030
U-2 OS cells	ATCC	Cat #HTB-96; RRID: CVCL_0042
Oligonucleotides		
CELSR2 validation For: 5'-TGCC ATTCTGTCCTTCGATT-3'	This study	N/A
CELSR2 validation Rev: 5'-TCAG AGAGGTGGTGTGATGC-3'	This study	N/A
CEP135 validation For: 5'-AGAC CCAGAAAGTTCCCCAA-3'	This study	N/A
CEP135 validation Rev: 5'-TGGA TGACAGAAAAGGAGAGG-3'	This study	N/A
DYNC1I2 validation For: 5'-TTCA TTATTGCCCGCACATT-3'	This study	N/A
DYNC1I2 validation Rev: 5'-TCCC TAAGAAAACATGCCAAAA-3'	This study	N/A
KIAA1614 validation For: 5'-TCCT CAGCCCTGGTCATCTA-3'	This study	N/A
KIAA1614 validation Rev: 5'-CAGG CTTGGTTCACAGTCTAGGG-3'	This study	N/A
LRP1B validation For: 5'-TCTCCA ATTTTGTTGGAAATATCA-3'	This study	N/A
LRP1B validation Rev: 5'-GTGACA TGGATGGGATGAAC-3'	This study	N/A
MAP7 validation For: 5'-TTATCAC CTCCTCCCTCTCAG-3'	This study	N/A
MAP7 validation Rev: 5'-TGGTTTT GTTCTTGGATTTG-3'	This study	N/A
MR1 validation For: 5'-GACAGGT GGGCTTCCATAAG-3'	This study	N/A
MR1 validation Rev: 5'-TGTCAAG ATGCTGCTCAAAG-3'	This study	N/A
NOL6 validation For: 5'-CCCCAA GACCCTTACCTCTT-3'	This study	N/A

(Continued on next page)

***Continued***

REAGENT or RESOURCE	SOURCE	IDENTIFIER
NOL6 validation Rev: 5'-TCCACC AAAGCACAAAGACTC-3'	This study	N/A
PITPNM2 validation For: 5'-CACC CTCACCCCTCAAGACAAG-3'	This study	N/A
PITPNM2 validation Rev: 5'-GGAC ACTGGAGAAGGGGTCA-3'	This study	N/A
POLR3C validation For: 5'-ACAC GATGTCTGGCACATA-3'	This study	N/A
POLR3C validation Rev: 5'-ATGGA GGGTCAGTATGGTATCC-3'	This study	N/A
PPP1R3E validation For: 5'-GGATG GAGATGGGTGCTCTT-3'	This study	N/A
PPP1R3E validation Rev: 5'-CTGG AGGTGTCCTGCAAGGAG-3'	This study	N/A
PPRC1 validation For: 5'-TACCCC TCCCCACCAGTT-3'	This study	N/A
PPRC1 validation Rev: 5'-TGCAG GCTTTTCGGTAACAG-3'	This study	N/A
PRMT9 validation For: 5'-TGAGG TCCAGAGCAATACGA-3'	This study	N/A
PRMT9 validation Rev: 5'-GGCTA GATGGAGGATGGAGA-3'	This study	N/A
SNCG validation For: 5'-TGGTCT CTGCCTTCCTATCC-3'	This study	N/A
SNCG validation Rev: 5'-TAACTG GGCACTCACCCCTT-3'	This study	N/A
TIA1 exon11 For: 5'-CTGCAATCC ATGAAACACCA-3'	This study	N/A
TIA1 exon11 Rev: 5'-GAAGTTGC CCCAGAACTACAAGA-3'	This study	N/A
TIA1 exon12 For: 5'-TTTTTATTTC CAGTGTGTTTTCA-3'	This study	N/A
TIA1 exon12 Rev: 5'-GATGATGG CCCTGTGTGTTT-3'	This study	N/A
TIA1 exon13 For: 5'-CATCCAGCA TCTTGTTCCTTTT-3'	This study	N/A
TIA1 exon13 Rev: 5'-CAAGGCAT AGAGATGAGATGGA-3'	This study	N/A
P362L mut For: 5'-CAAATTATGGAG TGCAACTGCCTCAAGGGCAAATG-3'	This study	N/A
P362L mut Rev: 5'-CATTTCGCCCTT GAGGCAGTTGCACTCCATAATTG-3'	This study	N/A
A381T mut For: 5'-CTGGGTATCGAG TGACAGGGTATGAAACC-3'	This study	N/A
A381T mut Rev: 5'-GGTTTCATACCC TGTCACTCGATACCCAG-3'	This study	N/A
E384K mut For: 5'-GTGGCAGGGTA TAAAACCCAGACGCG-3'	This study	N/A
E384K mut Rev: 5'-CGCGTCTGGGT TTTATACCCCTGCCAC-3'	This study	N/A
SureSelect forward primers	Agilent	Cat #5190-3620
SureSelect Pre-Capture indexing reverse primers	Agilent	Cat #5792-3694

(Continued on next page)

***Continued***

REAGENT or RESOURCE	SOURCE	IDENTIFIER
<b>Recombinant DNA</b>		
pEGFP-C1 vector	Clontech	Cat #632470
pEGFP-C1-TIA1 wild-type	This study	N/A
pEGFP-C1-TIA1 P362L	This study	N/A
pEGFP-C1-TIA1 A381T	This study	N/A
pEGFP-C1-TIA1 E384K	This study	N/A
Untagged TIA1 wild-type	This study	N/A
mCherry vector	This study	N/A
pETite N-His SUMO Kan vector	Lucigen Corporation	Cat #49003-1
pETite N-His SUMO TIA1 wild-type	This study	N/A
pETite N-His SUMO TIA1 P362L	This study	N/A
pETite N-His SUMO TIA1 A381T	This study	N/A
pETite N-His SUMO TIA1 E384K	This study	N/A
TdTOMATO TDP-43	Addgene	Cat #28205
<b>Software and Algorithms</b>		
CellProfiler Software	The Broad Institute of Harvard and MIT	<a href="http://cellprofiler.org/">http://cellprofiler.org/</a>
GraphPad Prism v6 Software	GraphPad	<a href="https://www.graphpad.com/scientific-software/prism/">https://www.graphpad.com/scientific-software/prism/</a>
HiSeq Data Collection v2.0.12	Source	N/A
Igor Pro 6	Wavemetrics	<a href="https://www.wavemetrics.com/">https://www.wavemetrics.com/</a>
Illumina cBot Software	Illumina	N/A
Illumina Real Time Analysis (RTA) Software v1.17.21.3	Illumina	N/A
ImageJ 1.46r Software	NIH	<a href="https://imagej.nih.gov/ij/download.html">https://imagej.nih.gov/ij/download.html</a>
Sequencher v4.8 Software	Gene Codes Corporation	<a href="http://www.genecodes.com/free-download">http://www.genecodes.com/free-download</a>
Slidebook Software	Intelligent Imaging Innovations	<a href="https://www.intelligent-imaging.com/slideshow">https://www.intelligent-imaging.com/slideshow</a>
<b>Other</b>		
ANNOVAR	Wang et al., 2010	<a href="http://annovar.openbioinformatics.org/en/latest/">http://annovar.openbioinformatics.org/en/latest/</a>
CADD Webinterface	N/A	<a href="https://cadd.gs.washington.edu/">https://cadd.gs.washington.edu/</a>
GENESIS 2.0 Pipeline Platform	Gonzalez et al., 2015	<a href="https://www.genesis-app.com/#/dashboard">https://www.genesis-app.com/#/dashboard</a>
Genome Analysis Toolkit	Broad Institute	<a href="https://software.broadinstitute.org/gatk/">https://software.broadinstitute.org/gatk/</a>
SNP-Set (Sequence) Kernel Association Test (SKAT) R package	Wu et al., 2011	<a href="https://cran.r-project.org/web/packages/SKAT/index.html">https://cran.r-project.org/web/packages/SKAT/index.html</a>

**CONTACT FOR REAGENT AND RESOURCE SHARING**

Further information and requests for resources and reagents should be directed to and will be fulfilled by the Lead Contact, J. Paul Taylor ([jpaul.taylor@stjude.org](mailto:jpaul.taylor@stjude.org)).

**EXPERIMENTAL MODEL AND SUBJECT DETAILS****Study Populations**

One ALS/FTD family (UBCU2) and an ALS case-control association cohort were included in this study. All individuals agreed to be in the study and biological samples were obtained after informed consent from subjects and/or their proxies. UBCU2 is a multigenerational family of Irish/German and other European ancestry, with a family history of ALS and ALS with dementia. The proband (UBCU2-1) developed progressive limb weakness and hyper-reflexia at age 51, followed by a change in personality and behavior at age 54. She died at age 55 with a clinical diagnosis of ALS with early behavioral variant frontotemporal dementia (bvFTD). A niece of the proband (UBCU2-14) presented with childhood dyslexia and developed changes in personality and expressive aphasia at

age 28, followed by bulbar and limb weakness a few months later. She suffered severe deterioration in language and cognition and progressive weakness during the final year and died at age 30 with a clinical diagnosis of FTD with probable ALS. The sister of the proband (UBCU2-2) displayed mild memory problems when assessed at age 56.

For the genetic association studies, we analyzed DNA samples of 1039 unrelated ALS patients (584 male, 455 female) available in our laboratory, including 38 with a diagnosis of FTD in addition to ALS (20 male, 18 female). All patients were of self-reported non-Hispanic white ancestry. The average age at diagnosis was  $60.0 \pm 11.7$  years (range 19–88). A positive family history of ALS in a first or second degree relative was reported in 136 patients (13.1%). Patients underwent a full neurological evaluation including electromyography, clinical laboratory testing, and imaging as appropriate to establish the clinical diagnosis of ALS and were recruited from eight centers: Mayo Clinic Jacksonville (n = 612), University of British Columbia, Canada (n = 171), University of Pittsburgh School of Medicine (n = 71), Coriell Institute for Medical Research (n = 75), University of Chicago Medicine (n = 57), Drexel University College of Medicine (n = 28), Northwestern University Feinberg School of Medicine (n = 10), University of Toronto, Canada (n = 11), and the University of Western Ontario, Canada (n = 4). Patients with ALS ± FTD were compared to a group of 3036 controls free of neurodegenerative disease (1442 male, 1594 female) for genetic association studies. The mean age at blood draw for controls was  $64.0 \pm 15.3$  years (range 20–99). All controls were of non-Hispanic white ancestry ascertained at Mayo Clinic Jacksonville (n = 1071), Mayo Clinic Rochester (n = 1738; of which 959 from the Mayo Clinic Biobank) and Mayo Clinic Scottsdale (n = 227). All patients signed informed consent and this study was approved by the ethics committee of all respective institutions.

### Mammalian Cell Culture

HeLa cells (of female origin) were grown and maintained in DMEM High Glucose (Hyclone SH30022.01) medium supplemented with 10% fetal bovine serum. Cells were passaged and plated using 1X TrypLE Express (Thermo Fisher Scientific). Cells were authenticated by short tandem repeat (STR) profiling.

### Bacterial Cell Culture

cDNA clones were transformed into One Shot TOP10 chemically competent *E. coli* (Thermo Fisher Scientific). Single colonies were grown overnight at  $37^{\circ}\text{C}$  in LB media containing selection antibiotic at a concentration of 50  $\mu\text{g}/\text{ml}$ . Cells were pelleted by centrifugation and lysed for harvesting DNA. All competent bacterial cells [One Shot TOP10 and BL21(DE3) SOLOS] were stored at  $-80^{\circ}\text{C}$  until transformation for cloning and recombinant protein expression.

## METHOD DETAILS

### Whole Exome Sequencing and Variant Calling

Paired-end indexed libraries were prepared using the Agilent Bravo liquid handler following the manufacturer's protocol (Agilent Technologies). Briefly, 1  $\mu\text{g}$  of genomic DNA (gDNA) was fragmented using the Covaris E210 Sonicator. The settings of duty cycle 10%, intensity 5, cycles 200, time 360 s generated double-stranded DNA fragments with blunt or sticky ends with a fragment size mode of 150–200bp. The ends were repaired and phosphorylated using Klenow, T4 polymerase, and T4 polynucleotide kinase, after which an "A" base was added to the 3' ends of double-stranded DNA using Klenow exo- (3' to 5' exo minus). Paired-end Index DNA adaptors (Agilent) with a single "T" base overhang at the 3' end were ligated, and the resulting constructs were purified using AMPure SPRI beads from Agencourt (Beckman Coulter Genomics). The adaptor-modified DNA fragments were enriched by 4 cycles of polymerase chain reaction (PCR) using SureSelect forward and SureSelect Pre-Capture indexing reverse (Agilent) primers. The concentration and size distribution of the libraries was determined via Agilent Bioanalyzer DNA 1000 chip.

Whole exome capture of 75Mb was carried out using the Agilent Bravo liquid handler following the protocol for Agilent's SureSelect XT Human Exome + UTR v5. 750 ng of the prepped library was incubated with whole exon biotinylated RNA capture baits supplied in the kit for 24 hr at  $65^{\circ}\text{C}$ . The captured DNA:RNA hybrids were recovered using Dynabeads MyOne Streptavidin T1 (Life Technologies). The DNA was eluted from the beads and purified using Ampure XP (Beckman Coulter Genomics). The purified capture products were then amplified using the SureSelect Post-Capture indexing forward and index PCR reverse primers (Agilent) for 12 cycles. Libraries were validated and quantified on the Agilent Bioanalyzer.

Libraries were pooled at equimolar concentrations in batches of three samples and loaded onto paired end flow cells at concentrations of 11 pM to generate cluster densities of 600,000–800,000/mm<sup>2</sup> following Illumina's standard protocol using the Illumina cBot and HiSeq paired-end cluster kit version 3 (Illumina). The flow cells were sequenced as 101 X 2 paired end reads on an Illumina HiSeq 2000 using TruSeq SBS sequencing kit version 3 and HiSeq data collection version 2.0.12 software. Base-calling was performed using Illumina's RTA version 1.17.21.3. FastQ files were processed into the GENESIS pipeline (Gonzalez et al., 2015).

### Filtering of Variants

Filtering of variants was performed in the GENESIS web application [Innovative genomic collaboration using the GENESIS (GEM.app) platform] (Gonzalez et al., 2015). Variants affecting protein sequence such as splice-site, missense, non-sense and frameshift variants were selected when present heterozygous in the two affected members of family UBCU2. Furthermore, variants were only retained when both were absent from the Exome Variant Server (EVS; <http://evs.gs.washington.edu/EVS/>) population, present two times or less in Exome Aggregation Consortium (ExAC; <http://exac.broadinstitute.org/>) and the gene harboring the variant is

expressed in brain tissue based on the GTEx database (<https://gtexportal.org/>). The remaining 15 variants were annotated using ANNOVAR (Wang et al., 2010).

### Variant Confirmation and *TIA1* Screening

For sequence validation of variants identified by exome sequencing, specific primers were designed surrounding each rare variant shared by UBCU2-1 and UBCU2-14. DNA fragments were amplified using Apex products, purified using the Agencourt Ampure system (Beckman Coulter Genomics), and sequenced using Big Dye Terminator V3.1 (Applied Biosystems). Sequencing products were then purified with CleanSEQ (Beckman Coulter Genomics) and then run on an ABI3730xl Genetic Analyzer (Thermo Fisher Scientific). Sequences were analyzed using Sequencher 4.8 software (Gene Codes Corporation). *TIA1* exons 11, 12 and 13 encoding the prion-like domain of TIA1 were sequenced from human gDNA in all 1045 patients from our association cohort and in 2077 controls. The remaining 959 controls from the Mayo Clinic Biobank were analyzed for coding *TIA1* mutations using recently generated whole genome sequences generated on the HiSeq X Ten System (HudsonAlpha) and analyzed using our in-house developed GenomeGPS v4.0 pipeline with BWA-MEM alignment to hg38 reference and variant calling using Genome Analysis Toolkit (Broad Institute). CADD scores for *TIA1* variants identified in the additional ALS/FTD patients were generated using CADD web interface (<https://cadd.gs.washington.edu/>).

### Mutagenesis

Mutations for *TIA1* were created by using the site-directed mutagenesis kit (Agilent). *TIA1* wild-type and mutants were subsequently cloned into pEGFP-C1 vector at BsrG1 and EcoRI site as a fusion gene without affecting the original reading frame of EGFP-C1. All clones were verified by restriction enzyme digestion and sequence analysis.

### Immunofluorescence

HeLa cells were seeded on 8-well glass slides (Millipore). Cells were transfected 24 hr after seeding using FuGene 6 (Promega) with GFP-TIA1-WT, GFP-TIA1-P362L, GFP-TIA1-A381T, or GFP-TIA1-E384K construct. 48 hr post transfection, cells were stressed with 500 µM sodium arsenite (Sigma-Aldrich) for 30 min. Cells were then fixed with 4% paraformaldehyde (Electron Microscopy Sciences), permeabilized with 0.5% Triton X-100, and blocked in 3% bovine serum albumin (BSA). Primary antibodies used were against C-terminal TDP-43 (12892-1-AP; ProteinTech) and G3BP1 (611127; BD Biosciences). For visualization, the appropriate host-specific Alexa Fluor 555 or 647 (Molecular Probes) secondary antibody was used. Slides were mounted using Prolong Gold Antifade Reagent with DAPI (Life Technologies). Images were captured using a Leica TCS SP8 STED 3X confocal microscope (Leica Biosystems) with a 63x objective.

Double label immunofluorescence was performed on 5-µm thick sections of formalin-fixed, paraffin-embedded post-mortem human spinal cord tissue from cases with *TIA1* mutations (UBC2-1, UBC2-14, NWU-1 and ALS752-1), ALS/FTD patients without *TIA1* mutations (N = 2) and a neurologically normal control subject. Tissue sections were heated to 60°C for 20 min, then immediately deparaffinized and rehydrated. Antigen retrieval was performed in citrate buffer (10 mM, pH 6.0, 10 min at 95°C in a water bath). The sections were blocked for 1 hr with 5% donkey serum in 0.1% Triton X-100 in TBS. Incubation with various combinations of primary antibodies (rat anti-phosphorylated TDP-43 from M. Neumann (1:1000) (Neumann et al., 2009) combined with one of three anti-TIA1 antibodies: Santa Cruz goat anti-TIA1, 1:300; Santa Cruz rabbit anti-TIA1, 1:300; Proteintech rabbit anti-TIA1, 1:100) was performed in the same blocking solution overnight at 4°C. The sections were then washed, and incubated with appropriate Alexa Fluor- or biotin-conjugated secondary antibodies at 1:1000 dilution for 1 hr at room temperature. Where needed, a third step with Alexa Fluor-conjugated streptavidin (1:1000) was added for 40 min. Background fluorescence was then quenched by staining with 0.1% Sudan Black in 70% ethanol for 15 min. Slides were mounted after 15 min incubation in DAPI with Prolong-Gold anti-fade reagent (Invitrogen). Microscopy was performed using a Nikon Eclipse i-80 epifluorescent microscope and NIS-Elements software. Images were further processed and merged using ImageJ.

### Live-Cell Time-Lapse Imaging and Fluorescence Recovery After Photobleaching

HeLa cells (ATCC) were seeded on sterilized 40mm #1.5 thick coverslips (Bioparts). Cells were transfected 24 hr after seeding using FuGene 6 (Promega) with 0.5 µg GFP-TIA1-WT, GFP-TIA1-P362L, GFP-TIA1-A381T, GFP-TIA1-E384K, or wild-type TDP-43-TdTO MATO construct. 48 hr post transfection, the coverslip was transferred to a FCS2 chamber, assembled according to the manufacturer's instructions (Bioparts). Media was perfused through the chamber, and then the chamber was placed into a Marianas Spinning Disk Confocal system with a stage-top incubator and 63x objective with an objective heater (Bioparts), both preheated to 37°C. The Microaque duct Slide heater (part of the FCS2 system) was set to 37°C, and the heated objective with 37°C immersion oil (Zeiss) was raised until it immersed the coverslip, and the system was left to equilibrate for 10 min after both the Microaque duct Slide and objective heaters read 37°C.

For time-lapse imaging, using SlideBook software with definite focus engaged, multipoint images were taken every 20 s with the 488 nm laser at 30% power. Two minutes into imaging, both the Microaque duct Slide and Objective temperatures were raised to 43°C to begin heat shock. 30 min later, both were lowered back to 37°C to alleviate the stress and were imaged until granules disappeared or after 3-4 hr passed. 250-500 µL fresh media was perfused through the chamber at every hour of imaging.

For fluorescence recovery after photobleaching, using SlideBook software with continuous definite focus engaged, images were taken every 500 ms with the 561 nm laser at 15% power for 87.5 s. 5 frames into imaging cytoplasmic regions were photobleached at 50% 561nm FRAP laserstack power for 1ms. The microaquect slide and objective heaters were raised to 43°C to induce stress granules and the stress granules were photobleached under the same conditions as the cytoplasmic regions prior to stress. Recovery curves were normalized to background fluorescence for subtracting noise, and adjacent non-bleached cells for fluorescence intensity fluctuations. Half recovery time and mobile fraction at the end of 87.5 s were empirically calculated. Average and standard errors were calculated from fifteen individual traces for cytoplasmic regions before heat shock, sixteen individual traces in SGs and twenty three individual traces in cytoplasmic regions after heat shock.

### Recombinant TIA1 Cloning and Purification

Purification of TIA1 was followed as given in [Lee et al. \(2016\)](#). Recombinant DNA for TIA1 wild-type, E384K, P362L and A381T constructs were cloned into pETTite N-His SUMO Kan vector (Lucigen Corporation). Plasmids were chemically transformed into BL21\_DE3 cells (Lucigen Corporation). A single bacterial colony, from a Luria-Broth (LB) agar plate with 600 µg/ml of kanamycin was grown overnight at 37°C, in 50 mL LB medium with 600 µg/ml of Kanamycin (LB-Kan), shaking at 200 rpm (New Brunswick Innova 44R shaker). Saturated overnight culture was transformed into two 2.5 L baffled flasks, each of 1 L LB medium with Kanamycin. Cell density, measured by OD600, was allowed to reach 0.5 by shaking at 37°C. After inducing with 500 µM isopropyl β-D-1-thiogalactopyranoside (IPTG), expression was done for 20 hr at 16°C.

Cells were pelleted at 4000 × g for 20 min at 4°C. Pellets from 1 L of cell culture were resuspended and solubilized in 50 mL of 50 mM HEPES, pH 7.5, 2 mM dithiothreitol (DTT), 250 mM NaCl buffer with cOmplete, Mini, EDTA-free protease inhibitor cocktail (Sigma-Aldrich). Resuspended cells were lysed by passing through a LM10 microfluidizer (Microfluidics) at 18,000 psi. Cell debris were pelleted at 17,000 × g at 4°C for 1 hr and the supernatant was decanted and filtered through a 0.45 micron PVDF membrane. Supernatant was loaded onto a HisTrap FF Ni-column (GE Healthcare), washed with lysis buffer, and eluted with 300 mM imidazole. The proteins were treated with 0.2 mg/ml RNase A (Roche) for 15 min at 37°C. His-SUMO-TIA1, with a calculated isoelectric point of 6.5, was purified by ion exchange chromatography with a HiTrap Q column (GE Healthcare) using a salt gradient from 75 mM to 500 mM NaCl. The fractions were analyzed by SDS-PAGE gel, pooled, and concentrated. They were then subjected to size exclusion chromatography on a Superdex 200 16/60 column (GE Healthcare) equilibrated in 50 mM HEPES, pH 7.5, 400 mM NaCl, and 5 mM DTT. The fractions were analyzed by SDS-PAGE gel, pooled, concentrated, and stored at –80°C. Absence of RNA was confirmed by TBE Urea gel electrophoresis and 260/280 absorbance ratio. Proteins were labeled with Oregon Green and Texas Red using Molecular Probes Protein Labeling Kits.

### Phase Separation

Protocol from [Elbaum-Garfinkle et al. \(2015\)](#) was modified to obtain the phase diagram (also known as co-existence line of T versus concentration of dilute phase) of TIA1 variants. Purified proteins were diluted to 15 µM, 150 mM NaCl with 50 mM HEPES at pH 7.5. Dilution of salt from 400 mM NaCl (storage buffer) to 150 mM NaCl induced phase separation. Samples were filtered through a 0.22 micron PVDF membrane to get rid of aggregates, and incubated at six different temperatures (5, 10, 15, 20, 25 and 30°C) for 30 min. After equilibration at six different temperatures, samples were centrifuged at their respective temperatures at 21,000 × g for 7 min. Experiments were performed in six replicates for wild-type and P362L, and thrice for A381T and E384K to obtain the average and standard error of the mean (SEM). Curves were fit to data using a quadratic equation ( $R^2$  wild-type = 0.99;  $R^2$  P362L = 0.99;  $R^2$  A381T = 0.97;  $R^2$  E384K = 0.99). Light or protein-depleted phase was decanted, and concentration was measured using a NanoDrop at 280 nm with molar extinction coefficient of His-SUMO-TIA1 calculated as 82195 M-1 cm-1 ([Wilkins et al., 1999](#)). Standardization of protein concentration with respect to A280 was confirmed by SDS-PAGE. See also [Figure S3](#).

### In Vitro Fibrillization

Fibrillization was monitored by Thioflavin T (ThT) fluorescence at 480 nm. Filtered, phase separated samples of 20 µM of proteins and 5 µM ThT at 50 mM HEPES, pH 7.5, 5 mM DTT, 150 mM NaCl, were observed with a 100x oil objective through Leica SP8 confocal microscope. Kinetics of fibrillization was studied on a 96-well plate reader using filtered light phase (2.5 µM protein concentration) at room temperature. Samples were agitated on an Eppendorf Thermomixer C heat block at 300 rpm for 24 hr. ThT fluorescence at 480 nm was observed at 0 hr (defined as sample immediately after filtration), 2, 5, 8 and 24 hr. Baseline correction was performed using 2.5 µM BSA as a standard solution. Experiments were performed in six replicates for wild-type and P362L, and thrice for A381T and E384K to obtain average and SEM.

For transmission electron microscopy (TEM), reaction mixture (10 µl) of TIA1 wild-type or mutants, after 2 hr agitation at 300 rpm of 20 µM proteins, was directly deposited on a surface of a TEM grid (CF-400-Cu; Electron Microscopy Sciences). The surface of the grid was washed three times with 10 µL of distilled water. The grid was subsequently stained for a few seconds with a 10 µL drop of 2% uranyl acetate. After the uranyl acetate solution was blotted, the grid was dried in air. TEM images were obtained with a JEOL 1200EX electron microscope at 120 kV.

### Fluorescence Recovery After Photobleaching in Droplets

Droplets of 25  $\mu$ M protein samples (spiked with Oregon Green for wild-type, or Texas Red for P362L, A381T and E384K variants at a ratio of 1:1000 labeled to unlabeled protein) were observed on a Linkam PE100 thermal stage (at 20°C) mounted on a Marianas spinning disk confocal imaging system on a Zeiss Axio Observer inverted microscope platform. Droplets were photobleached using 70% FRAP laserstack power for 5 ms. Images were obtained every 300 ms to observe fluorescence recovery up to 225 s. Recovery curves were normalized to background fluorescence for subtracting noise, and adjacent non-bleached droplet for fluorescence intensity fluctuations. Half recovery time and mobile fraction at the end of 225 s were empirically calculated. Average and standard errors were calculated from six individual traces for wild-type and A381T, eight for P362L, and ten for E384K. All imaging was done on hydrophobic coverslips (HybriSlip; Molecular Probes) sandwiching Secure-Seal Imaging Spacers (0.12 mm depth).

### Human Tissue Solubility Assay

Urea fractions were prepared from human frontal cortex tissue as described previously with few modifications (Neumann et al., 2007; Zhang et al., 2007). Approximately 100 mg of brain tissue was homogenized in 500  $\mu$ L Tris-buffered saline (TBS) and centrifuged at 25,000  $\times$  g for 30 min at 4°C. Pellets were re-homogenized in 500  $\mu$ L TBS and re-centrifuged under the same conditions. Pellets were resuspended in TBS containing 1% Triton X-100 (TX buffer) and centrifuged at 180,000  $\times$  g for 30 min at 4°C. Pellets were again suspended in TX buffer supplemented with 30% sucrose and centrifuged at 180,000  $\times$  g for 30 min at 4°C. Pellets were re-homogenized in a 1% sarkosyl solution, after which samples rotated at room temperature for 1 hr. Samples were then centrifuged at 180,000  $\times$  g for 30 min at room temperature before re-extracting the remaining pellet in 50  $\mu$ L of 7M urea. All buffers, with the exception of urea, were supplemented with protease and phosphatase inhibitors. Urea-extracted samples were stored at –80°C until use.

### Cell Culture Solubility Assay

Solubility and biochemical analysis was performed as described in Kim et al. (2013) with several modifications. For each sample  $\sim 3 \times 10^6$  cells were washed twice with ice-cold 1x PBS and lysed in ice-cold RIPA buffer (25 mM Tris-HCl pH 7.6, 150mM NaCl, 1% NP-40, 1% sodium deoxycholate, 0.1% SDS; Thermo Fisher 89900). Cell lysates were then passed through a 21-gauge needle 10 times before being cleared by centrifugation at 100,000  $\times$  g for 30 min at 4°C to generate RIPA-soluble fraction. The pellets were washed twice with ice cold RIPA buffer and re-centrifuged for 10 min. RIPA-insoluble pellets were then extracted with urea buffer (7 M urea, 2 M thiourea, 4% CHAPS, 30 mM Tris, pH 8.5) by vortexing samples for 15 s every 10 min for 30 min while at room temperature. The samples were then centrifuged at 100,000 g for 30 min at 4°C. Halt Protease and Phosphatase Inhibitor (Thermo Fisher # 78443) was added to all buffers before use. Proteins were resolved by NuPAGE Novex 4%-12% Bis-Tris Gel (Invitrogen).

### Western Blotting

For human urea fractions, an equal volume of sample and Tris-glycine Novex buffer (Life Technologies; supplemented with 5%  $\beta$ -mercaptoethanol) were prepared for western blotting and were not further denatured. Samples were loaded into SDS polyacrylamide gels (Life Technologies) and electrophoresis was run at 80V. Protein was transferred onto an Immobilon PVDF membrane (Millipore) at 230 mA for 4 hr. Membranes were blocked for 1 hr in 5% dehydrated milk (prepared in TBS containing 0.05% Tween-20) before incubation with primary antibody. Horseradish peroxidase-conjugated secondary antibody (Promega) incubation followed by enhanced chemiluminescence was used for the detection of proteins. Primary antibodies used were goat anti-TIA1 (1:2,000; Santa Cruz), phosphorylated TDP-43 (1:1000), and rabbit anti-TDP-43 (1:10,000; ProteinTech).

### Histology

Human tissues were stained with hematoxylin and eosin (HE), HE combined with Luxol fast blue (HE/LFB) and Bielschowsky silver method.

### Immunohistochemistry (IHC)

Standard IHC was performed on 5- $\mu$ m thick human tissue sections using the Ventana BenchMark XT automated staining system (Ventana) and developed with aminoethylcarbazole (AEC). The primary antibodies employed were as follows: ubiquitin (DAKO; 1:500 following microwave antigen retrieval), p62 Lck ligand (BD Biosciences; 1:500 following microwave antigen retrieval), TDP-43 (ProteinTech; 1:1,000 following microwave antigen retrieval), hyperphosphorylated tau (clone AT-8; Innogenetics, Ghent, Belgium; 1:2,000 following microwave antigen retrieval),  $\alpha$ -synuclein (Thermo Scientific; 1:10,000 following microwave antigen retrieval), anti-beta amyloid (A $\beta$ ; DAKO; 1:100 with initial incubation for 3 hr at room temperature), and FUS (Sigma-Aldrich; 1:200, initial overnight incubation at room temperature, following microwave antigen retrieval).

IHC was also performed on sections of spinal cord and frontal cortex from *TIA1* mutation carriers, sporadic ALS patients in whom *TIA1* mutations were excluded, and normal control subjects using a number of commercial antibodies raised against various N-terminal and C-terminal epitopes of human TIA1, including: ProteinTech TIA1 (rabbit polyclonal against aa 1-214; 1:50, overnight incubation following microwave antigen retrieval), Santa Cruz TIA-1/TIAR (clone H-120; rabbit polyclonal against aa 21-140; 1:200, overnight incubation following microwave antigen retrieval), Santa Cruz TIA-1/TIAR (clone D-9; mouse monoclonal against aa 21-140; 1:200, overnight incubation following microwave antigen retrieval), Santa Cruz TIA1 (clone C-20; goat polyclonal raised against the TIA1 C terminus; 1:5000 following steaming antigen retrieval in sodium citrate buffer, pH 6), Abcam TIA1 ab40693 (rabbit

polyclonal antibody raised against aa 350-C terminus; 1:500 following microwave antigen retrieval), Abcam TIA1 ab140595 (rabbit monoclonal antibody against aa 350-C terminus; 1:100, overnight incubation) and Beckman Coulter TIA1 (IM2550; mouse monoclonal raised against human leukemia cells; 1:400 following heat retrieval).

## QUANTIFICATION AND STATISTICAL ANALYSIS

### Genetic Statistical Analyses

Gene-based analyses were performed using the SNP-set (Sequence) Kernel Association Test (SKAT) R package using variants with minor allele frequency < 0.0001 and adjusted for age and gender (Wu et al., 2011). We only tested *TIA1* and only rare variants in the LCD were included in the analysis based on the specific mutation identified by exome sequencing in family UBCU2 and prior functional evidence implicating LCDs of other RNA binding proteins in ALS-FTD. The  $8.7 \times 10^{-6}$  p value associated with rare *TIA1* LCD mutations is just short of exome-wide significance ( $p = 2.5 \times 10^{-6}$ ).

### Live-Cell Analysis

Live-cell imaging analysis was done manually, determining when granules appeared and disappeared for each cell. Only viable cells which were not rounded and which did not have spontaneous granules (puncta present prior to the 2 min mark in the video) were considered. For these cells, all of which being considered granule negative at the beginning of the video, were considered granule positive upon the frame at which distinct cytoplasmic puncta were visible. The frame at which no cytoplasmic puncta were visible any longer was when the cells were once again considered granule negative. Images were analyzed using SlideBook software. The percent of cells which were considered granule positive was determined and graphed at each time point ( $n = 24, 8, 19$ , and  $8$  videos for wild-type, P362L, A381T, and E384K, respectively). Two-way ANOVA with Dunnett's multiple comparisons test was performed using GraphPad Prism v6. A p value of less than 0.05 was used to determine significance.

### Automated Image Analysis

The same live-cell videos were subjected to automated puncta detection analysis using CellProfiler software (Broad Institute of Harvard and MIT). Individual frames of all movies were exported as tiff images and imported into the CellProfiler where each frame was individually analyzed. An automated analysis pipeline consisted of applying a “speckle” enhancement step prior to thresholding. A speckle is an area of enhanced intensity relative to its immediate neighborhood. The module enhances speckles using a white top-hat filter with a feature size of 10 pixels. After the speckle enhancement the granules were detected by applying adaptive “Robust Background” thresholding method. Adaptive strategy partitions the input image into tiles of 30 pixels and calculates thresholds for each tile. For each tile, the calculated threshold is applied only to the pixels within that tile. This approach is well suited for cells with varying intensity in the same movie (field of view). The Robust Background thresholding method applied within the tiles assumes that the background distribution approximates a Gaussian and trims the brightest and dimmest 5% of pixel intensities. It then calculates the mean and standard deviation of the remaining pixels and calculates the threshold as the mean + 3 times the standard deviation. Following the thresholding step all detected puncta were separated based on intensity and shape variation. Finally, the number and area of all segmented puncta objects were calculated and exported for making the graphs of the number and the average of area of SGs versus time using Microsoft Excel and/or Igor Pro (WaveMetrics). All graphs were normalized to maximum values. The purpose of these graphs is to show the behavior of the sample response to heat shock and supports our manual observation and analysis (Figure 2B). The fluorescence signal from each cell type was compared for one selected frame (Figure S2C) when cells had significant number of mature SGs.

### Phase Diagram, Fibrillation, and FRAP Analyses

Statistical analyses were performed using GraphPad Prism v6 or Microsoft Office Excel. All data are shown as the mean  $\pm$  standard error of the mean (SEM). The statistical significance of each variant compared to wild-type *TIA1* was investigated by Pearson correlation coefficient (Pearson's chi-square test), ordinary one-way ANOVA followed by Dunnett's multiple comparisons test, or two-way ANOVA followed by Dunnett's multiple comparisons test. The number of samples analyzed per experiment is provided in the corresponding figure legends. A p value of less than 0.05 was used to determine significance.

**Supplemental Information**

**TIA1 Mutations in Amyotrophic Lateral Sclerosis  
and Frontotemporal Dementia Promote Phase  
Separation and Alter Stress Granule Dynamics**

**Ian R. Mackenzie, Alexandra M. Nicholson, Mohona Sarkar, James Messing, Maria D. Purice, Cyril Pottier, Kavya Annu, Matt Baker, Ralph B. Perkerson, Aishe Kurti, Billie J. Matchett, Tanja Mittag, Jamshid Temirov, Ging-Yuek R. Hsiung, Charles Krieger, Melissa E. Murray, Masato Kato, John D. Fryer, Leonard Petrucelli, Lorne Zinman, Sandra Weintraub, Marsel Mesulam, Julia Keith, Sasha A. Zivkovic, Veronica Hirsch-Reinshagen, Raymond P. Roos, Stephan Züchner, Neill R. Graff-Radford, Ronald C. Petersen, Richard J. Caselli, Zbigniew K. Wszolek, Elizabeth Finger, Carol Lippa, David Lacomis, Heather Stewart, Dennis W. Dickson, Hong Joo Kim, Ekaterina Rogaeva, Eileen Bigio, Kevin B. Boylan, J. Paul Taylor, and Rosa Rademakers**

## Inventory of Supplemental Information

**Figure S1.** Related to Figure 1 and Table S3. Postmortem neuropathology of *TIA1* mutation carriers.

**Figure S2.** Related to Figure 2 and STAR Methods. Assessments of RNA contamination and protein standardization for recombinant TIA1, and fibrillization propensity of wild type and mutant TIA1.

**Figure S3.** Related to Figure 3. The GFP tag on TIA1 does not significantly alter its behavior in cells, nor the behavior of endogenous TIA1.

**Figure S4.** Related to Figure 3 and Figure 4. Automated live-cell image analysis and Recruitment of TDP-43 in TIA1-positive stress granules.

**Table S1.** Related to Figure 1. Validated shared variants between family members UBCU2-1 and UBCU2-14

**Table S2.** Related to Figure 1. Demographic and clinical features of *TIA1* mutation carriers

**Table S3.** Related to Figure 1 and Figure S1. Semi-quantitative grading of postmortem neuropathology in *TIA1* mutation carriers

**Video File.** Related to Figure 2. Live-cell Imaging Illustrates Prolongation of SG Recovery in Association with Disease-causing *TIA1* Mutations.

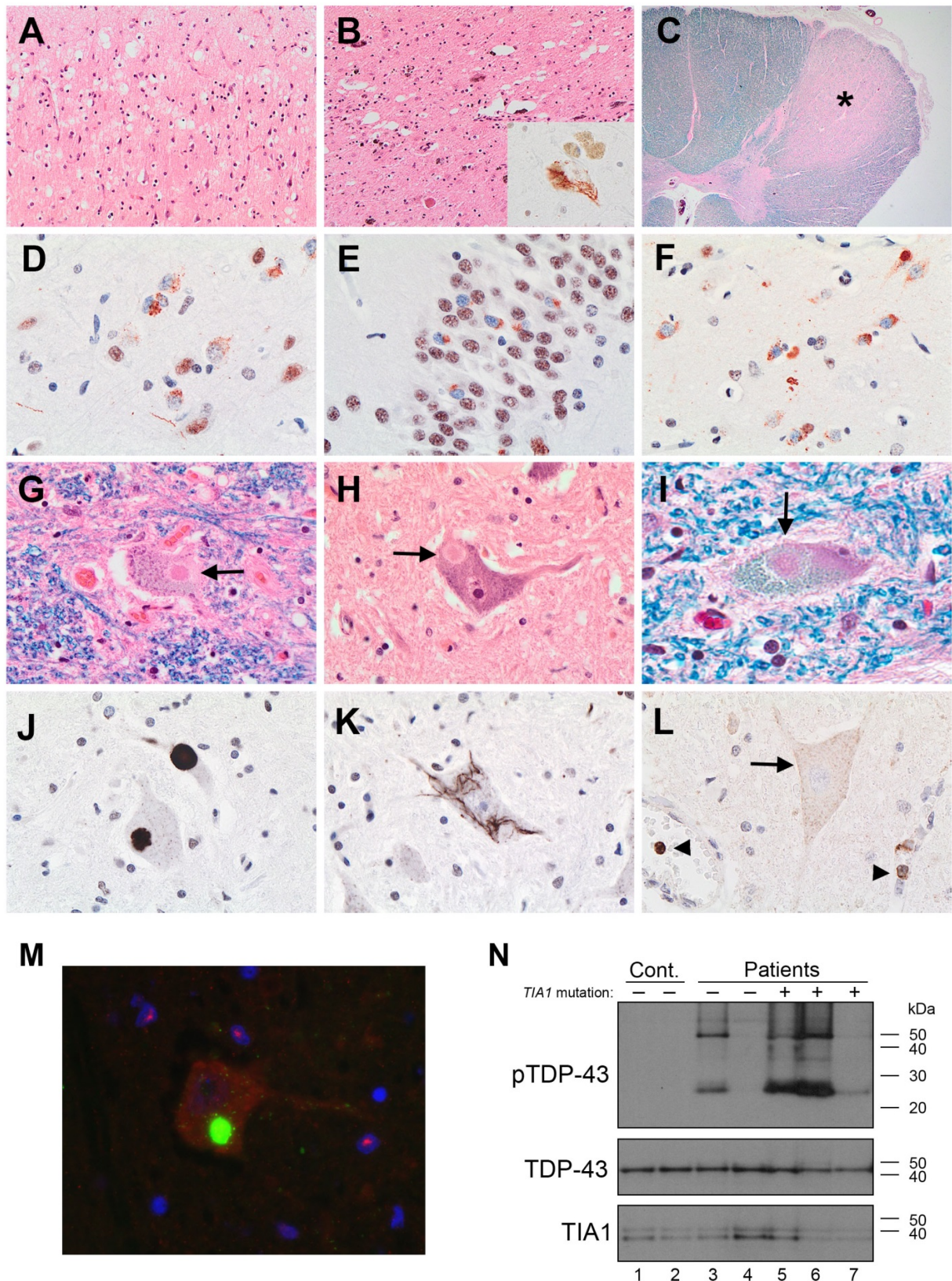


**Figure S1. Related to Figure 1 and Table S3. Postmortem neuropathology of *TIA1* mutation carriers.** All five *TIA1* mutation carriers who underwent autopsy examination had similar neuropathological findings. Chronic degenerative changes were most prominent in the premotor cerebral cortex (**A**), substantia nigra (**B**), corticospinal tracts (**C**, asterisk) and ventral grey matter of the spinal cord. In the cerebral neocortex, TDP-43 immunoreactive (-ir) neuronal cytoplasmic inclusions (NCI) were present in superficial and deep lamina, consistent with FTLD-TDP type B (**D**). TDP-43-ir NCIs were also common in the dentate granule cells of the hippocampus (**E**), the striatum (**F**) and pigmented neurons of the substantia nigra (**B**, inset). In all cases, some lower motors contained a large round hyaline NCI, often with a Lewy-body like appearance (**G-I**, arrows) that were TDP-43-ir (**J**). Diffuse granular and filamentous TDP-43-ir NCI were also present in lower motor neurons (**K**). IHC (**L**) and double label immunofluorescence (IF) (**M**) using a number of commercial antibodies that recognize various epitopes of TIA1 all showed delicate diffuse granular cytoplasmic staining of some large neurons (arrow) and more intense immunostaining of some lymphocytes (arrow heads) in sections from *TIA1* mutation carriers (**L**), ALS patients without *TIA1* mutations and normal controls, but did not demonstrate any specific pathological changes. Specifically, there was no evidence for co-localization of TIA1 (red) with the TDP-43-ir inclusions (green) in ALS patients with (**M**) or without *TIA1* mutations, nor was there an enrichment of insoluble TIA1 in the urea fraction obtained from the frontal cortex of *TIA1* mutation carriers (**N**). UBCU2-14, **A**, **B**, **C**, **D**, **F**, **H**, **K**; UBCU2-1, **E**, **G**, **L**; TOR-1, **I**; NWU-1, **J**. Hematoxylin and eosin (HE), **A**, **B** and **H**; HE and Luxol fast blue, **C**, **G** and **I**; TDP-43 IHC, **B** inset, **D**, **E**, **F**, **J** and **K**; TIA1 IHC, **L**; double label IF for TIA1 (red) and pTDP-43 (green) with nuclei stained with DAPI (blue), **M**. **N**: lanes 1 and 2, non-demented controls; lanes 3 and 4, ALS/FTD patients with no known genetic mutation; lane 5, UBCU2-1; lane 6, UBCU2-14; lane 7, ALS752-1.

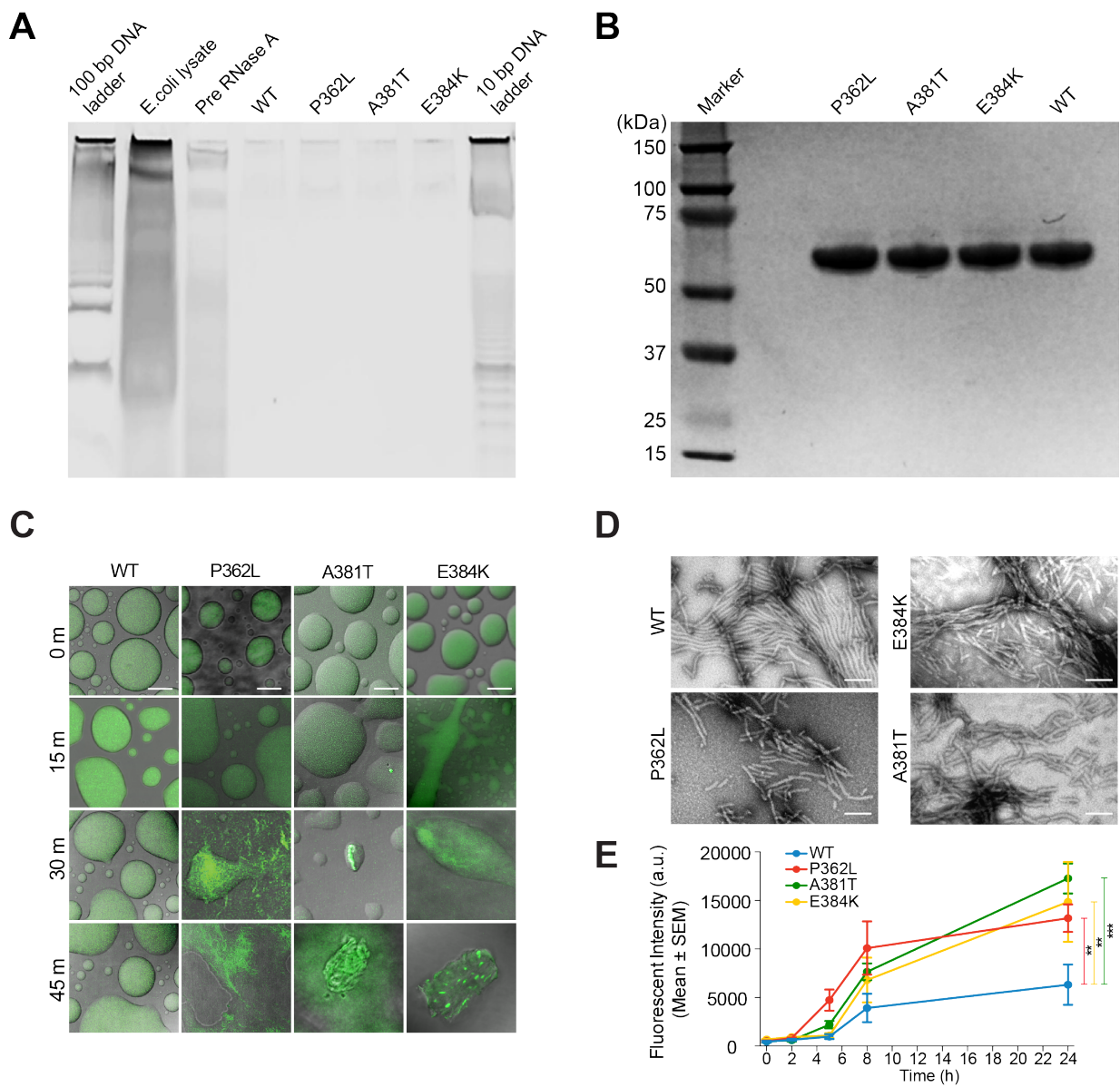


**Figure S2. Related to Figure 2 and STAR Methods. Assessments of RNA contamination and protein standardization for recombinant TIA1, and fibrillization propensity of wild type and mutant TIA1.** (A) A 15% Tris-Borate-EDTA (TBE)-Urea gel was run at 200 V with RNase free TBE buffer for 1 h. The gel was stained with SYBR® Gold nucleic acid stain indicating no RNA contamination in the purified TIA1 protein samples. (B) 4-12% Bis-Tris SDS PAGE shows equal protein quantity determined by absorbance of light at a wavelength of 280 nm (A280). All variants were normalized to an A280 of 0.1, and equal volume of samples was

loaded on each lane. (C) Merged DIC and fluorescent imaging illustrates the formation of ThT-positive aggregates formed in the dense phase of mutant (P362L, A381T, and E384K) TIA1. The dense phase was initiated by reducing the salt concentration to 150 mM NaCl. (D) TIA1 assembles into amyloid-like fibrils as illustrated by TEM. (E) TIA1 assembly into ThT-positive amyloid fibrils is accelerated by disease-causing missense mutations (P362L, A381T and E384K), as assessed by ThT fluorescence assay (see Extended Methods). Graph represents the mean  $\pm$  S.E.M.  $P^{**}<0.01$ ,  $P^{***}<0.001$  by two-way ANOVA with Tukey's multiple comparisons test. Scale bars: 10  $\mu$ m (C) and 200 nm (D).

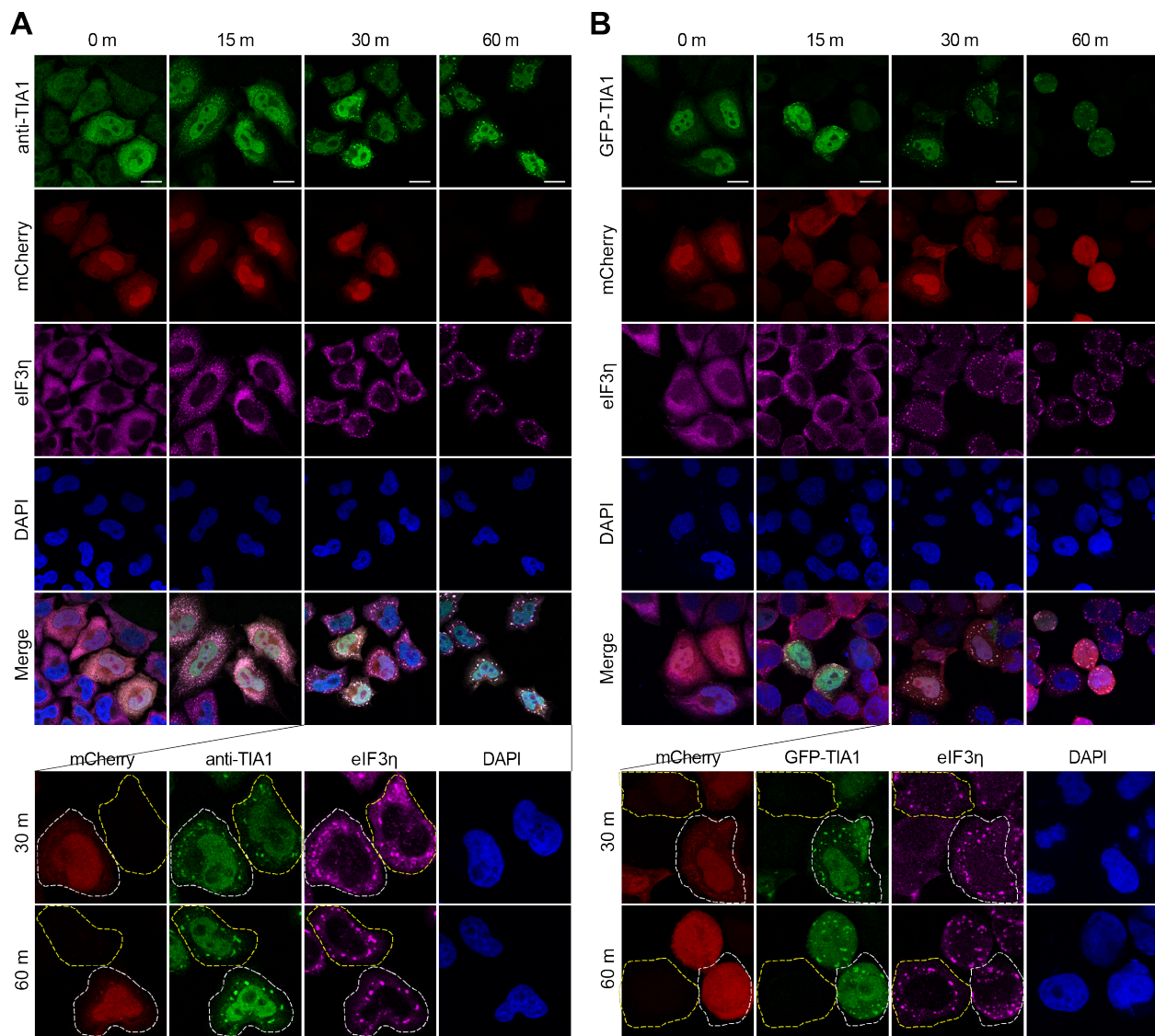


**Figure S3. Related to Figure 3. The GFP tag on TIA1 does not significantly alter its behavior in cells, nor the behavior of endogenous TIA1.** (A) HeLa cells were transfected with untagged wild-type TIA1 and mCherry as a transfection marker, treated with 0.5 mM sodium arsenite for the indicated time, and immunostained with anti-TIA1 (green) and anti-eIF $\eta$  (far-red). DAPI staining is shown in blue. Lower panel shows magnified images of cells at 30 min and 60 min post-arsenite treatment. Cells transfected with untagged TIA1 are indicated by a white dotted line; untransfected control cells in the same field are indicated by a yellow dotted line. (B) HeLa cells were transfected with GFP-tagged wild-type TIA1 and mCherry, treated with 0.5 mM sodium arsenite for the indicated time, and immunostained with anti-eIF $\eta$  (far-red).

DAPI staining is shown in blue. Lower panel shows magnified images of cells at 30 min and 60 min post-arsenite treatment. Cells transfected with GFP-TIA1 are indicated by a white dotted line; untransfected control cells in the same field are indicated by a yellow dotted line.

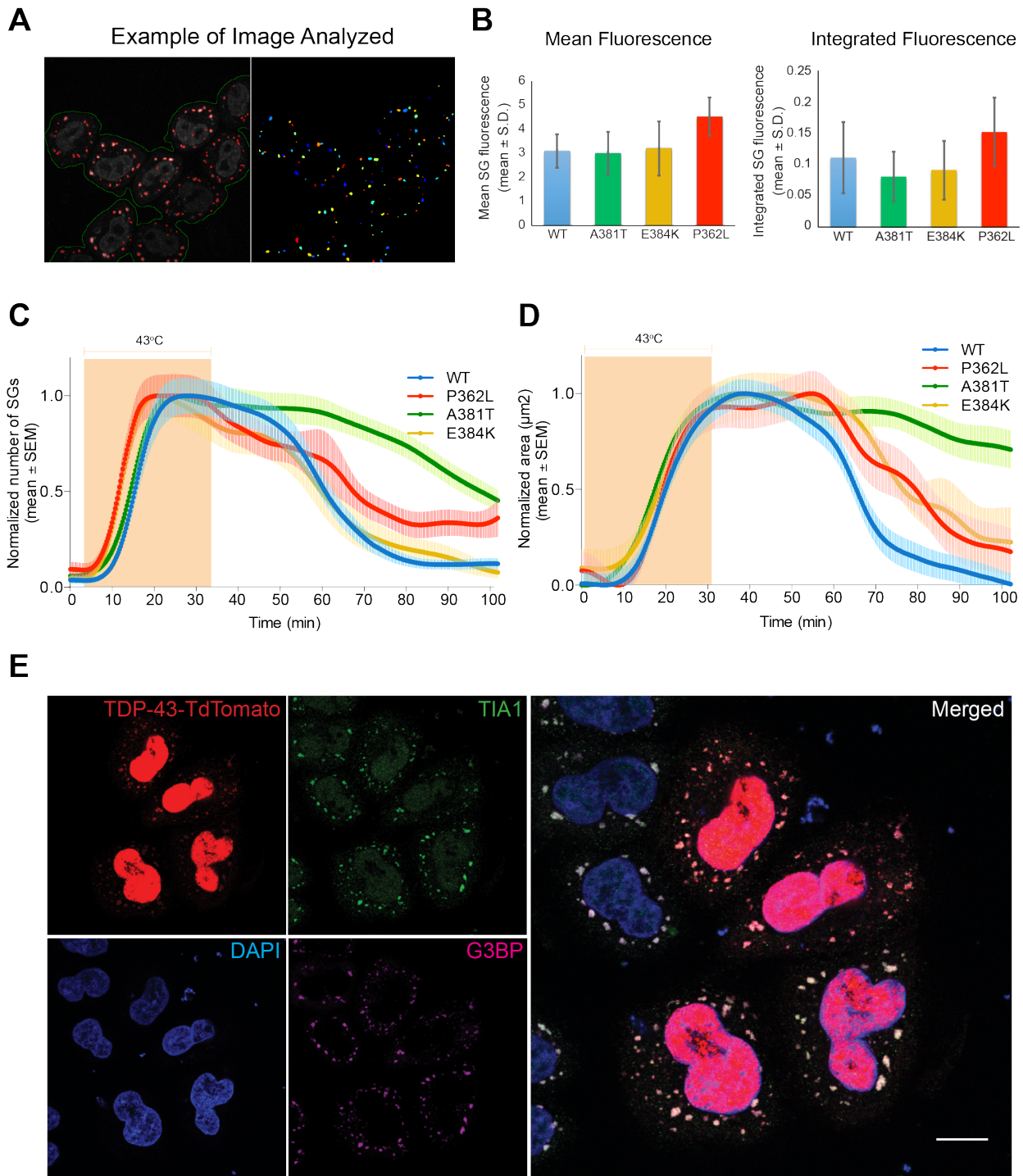


**Figure S4. Related to Figure 3 and Figure 4. Automated live-cell image analysis and Recruitment of TDP-43 in TIA1-positive stress granules.** (A) An example frame from a time-lapse movie showing a raw image (left) and segmented stress granule objects (right). The boundary of an area occupied by cells (green outline) and the outlines of segmented granules

are overlaid onto the raw image. **(B)** Mean and integrated fluorescence signal of all granules normalized to the mean (left) and integrated signal of non-granule region of cells (right) for the 40 min time frame, which corresponds to the state of cells with mature granules. Graphs represent the mean  $\pm$  S.D. **(C-D)** Number **(C)** and **(D)** average area of stress granules per cell over time normalized to maximum values. Graphs represent the mean  $\pm$  S.E.M. **(E)** Heat shock induced TDP-43-TdTomato puncta co-localize with SG components, including TIA1 and G3BP. Coverslip from experiment shown in Fig. 4B and 4C was immediately fixed and stained after FRAP analysis. Hela cells were stained with TIA1, G3BP, and DAPI. Scale bar = 10 um.

**Table S1. Related to Figure 1. Validated shared variants between family members UBCU2-1 and UBCU2-14**

Position	Gene Name	Brain Expression	HGVS cDNA Annotation	Protein Annotation	ExAC Allele Frequency	CADD phred	SIFT score	SIFT prediction	Polyphen2 HDIV score	Polyphen2 HDIV prediction	Mutation Taster score	Mutation Taster prediction	GERP ++ RS
chr12:123480003	<i>PITPNM2</i>	YES	NM_001300801:c.1987C>T	p.R663C	8.31E-06	32	0.002	D	1	D	1	D	3.9
chr2:172571882	<i>DYNC1I2</i>	YES	NM_001378:c.440A>G	p.D147G	3.65E-05	24.3	0.114	T	0.995	D	1	D	5.98
chr2:70439927	<i>TIA1</i>	YES	NM_022173:c.1085C>T	p.P362L	1.65E-05	24.1	0.005	D	0.967	D	1	D	5
chr10:88718460	<i>SNCG</i>	YES	NM_003087:c.6T>G	p.D2E		23.6	0.02	D	0.994	D	0.95	D	-9.87
chr2:141819672	<i>LRP1B</i>	YES	NM_018557:c.1184G>C	p.G395A		20.7	0.018	D	0	B	0.861	D	3.41
chr1:109807126	<i>CELSR2</i>	YES	NM_001408:c.5340C>A	p.S1780R		19.74	0.169	T	0.01	B	0.989	D	3.85
chr1:145608281	<i>POLR3C</i>	YES	NM_001303456:c.455T>C	p.M152T	1.67E-05	19.24							
chr9:33467244	<i>NOL6</i>	YES	NM_022917:c.1742A>G	p.Q581R		17.26	0.045	D	0.919	P	0.907	D	3.32
chr4:56874505	<i>CEP135</i>	Yes (low)	NM_025009:c.2293G>A	p.A765T		13.09	0.351	T	0.001	B	0.998	N	1.61
chr14:23771661	<i>PPP1R3E</i>	YES	NM_001276318:c.114_125del	p.Q38_P42del	0.0002	10.53							
chr1:180907781	<i>KIAA1614</i>	YES	NM_020950:c.2852C>A	p.S951Y		10.17	0.129	T	0.587	P	1	N	1.15
chr10:103906765	<i>PPRC1</i>	YES	NM_001288728:c.3656C>G	p.P1219R	8.25E-06	9.139	0.124	T	0.038	B	1	D	3.35
chr4:148575616	<i>PRMT9</i>	Yes (low)	NM_001304458:c.1093A>G	p.M365V	8.24E-06	2.309	0.568	T	0	B	1	D	4.85
chr1:181019419	<i>MR1</i>	Yes (low)	NM_001531:c.602_603del	p.T201fs									
chr6:136683761	<i>MAP7</i>	YES	NM_001198609:c.1440_1442dup	p.P481dup									

For each shared, confirmed variant in UBCU2-1 and UBCU2-14, the genomic position, gene name approved by the Hugo Gene Nomenclature Committee, brain expression based on GTEx database, cDNA annotation, protein annotation, ExAC allele frequency, CADD phred scores/SIFT/ Polyphen2/Mutation Taster scores and predictions and GERP++ score are provided when available. Variants with a CADD phred score higher than 20 are highlighted in bold. CADD, Combined Annotation Dependent Depletion; ExAC, Exome Aggregation Consortium; GERP, Genomic Evolutionary Rate Profiling; GTEx, Genotype-Tissue Expression; HDIV, human divergence; HGVS, Human Genome Variation Society; PolyPhen, Polymorphism Phenotyping; SIFT, Sorting Intolerant From Tolerant; RS, rejected substitution.

**Table S2. Related to Figure 1. Demographic and clinical features of *TIA1* mutation carriers**

Case	Sex	Race, Ethnicity	Onset (yrs)	Death or Current Age (yrs)	Presenting Symptom(s)	Final/Current clinical Diagnoses	Family History	Autopsy Findings	<i>TIA1</i> Mutation	ExAC Allele Frequency (Only European non-Finnish)	CADD phred
<sup>a</sup> UBCU2-1	F	white, non-Hispanic	51	55	limb weakness	ALS, early bvFTD	ALS, FTD, dementia	ALS, FTLD-TDP (B)	p.P362L	1.65E-05 (0)	24.1
<sup>a</sup> UBCU2-14	F	white, non-Hispanic	28	30	aphasia, personality change	FTD, probable ALS	ALS, FTD, dementia	ALS, FTLD-TDP (B)	p.P362L	1.65E-05 (0)	24.1
<sup>a</sup> UBCU2-2	F	white, non-Hispanic	55	55 (alive)	memory problems	CSND	ALS, FTD, dementia		p.P362L	1.65E-05 (0)	24.1
ALS458-1 (Mayo)	F	white, non-Hispanic	63	64 (alive)	bulbar weakness	ALS	ALS, Parkinson's		p.V294M	7.41E-05 (8.991E-05)	22.3
ALS701-1 (Mayo)	F	white, non-Hispanic	73	76	bulbar weakness	ALS, aphasia	none	NA	p.G355R	1.65E-05 (2.997E-05)	34
ALS752-1 (Mayo)	F	white, non-Hispanic	58	59	bulbar weakness	ALS	none	ALS, mild FTLD-TDP	p.V360M	4.12E-05 (5.994E-05)	23
NWU-1 (NWU)	F	white, non-Hispanic	65	68	aphasia	FTD (PPA), ALS	dementia	ALS, FTLD-TDP (B)	p.M334I	8.24E-06 (1.50E-05)	22.7
TOR-1 (Toronto)	F	white, non-Hispanic	73	79	aphasia	FTD (PNFA), ALS	none	ALS, FTLD-TDP (B)	p.A381T	8.24E-06 (1.498e-05)	22.4
Pitt-87 (Pittsburgh)	F	white, non-Hispanic	64	66	limb weakness	ALS	none	NA	p.A381T	8.24E-06 (1.498e-05)	22.4

Summary of the demographical, clinical, and pathological features observed in *TIA1* mutation carriers. ExAC allele frequency and CADD phred score are provided for each *TIA1* variant. ALS,

amyotrophic lateral sclerosis; bvFTD, behavioral variant FTD; CADD, Combined Annotation Dependent Depletion; CSND, clinically symptomatic but not demented; ExAC, Exome Aggregation Consortium; FTD, frontotemporal dementia; FTLD-TDP, frontotemporal lobar degeneration with TDP-43 immunoreactive pathology; NA, not available; PNFA, progressive nonfluent aphasia; PPA, primary progressive aphasia. <sup>a</sup>Members of the same family.

**Table S3. Related to Figure 1 and Figure S1. Semi-quantitative grading of postmortem neuropathology in *TIA1* mutation carriers**

		UBCU2-1		UBCU2-14		NWU-1		TOR-1		ALS752-1	
		ALS, early FTD		FTD, probable ALS		FTD, ALS		FTD, ALS		ALS	
		deg.	TDP-43	deg.	TDP-43	deg.	TDP-43	deg.	TDP-43	deg.	TDP-43
neocortex	motor	++	+	+	+	+	+	+	++	+	+++
	prefrontal	++	+++	+++	+++	++	+++	+	+++	-	++
	temporal	+	++	++	++	+	++	+	++	-	++
	parietal	+	++	++	++	-	+++	-	++	-	+
hippocampus	pyramidal	-	+	-	+	-	+	-	+	-	+
	dentate	-	++	-	++	++	++	+	+++	-	++
basal ganglia	caudate	+	+++	++	+++	+	+	-	++	-	+++
	putamen	-	+++	-	++	-	+	-	+	-	+
	GP	-	+	-	+	-	+	-	+	-	+
thalamus		-	-	-	+	+	+	-	-	-	+
midbrain	PAG	+	+	++	++	+	+	-	n/a	-	+
	SN	++	+++	+++	+++	+++	++	-	n/a	++	++
pons	basis	-	-	-	+	-	+	-	-	-	+
medulla	CN XII	++	++	+++	++	+++	++	++	+++	+++	++
spinal cord	CST	++	n/a	+++	n/a	++	n/a	+	n/a	++	n/a
	ant. horn	+++	+++	+++	+++	++	++	++	++	+++	+++
cerebellum	cortex	-	-	-	-	-	-	-	-	-	-
	dentate	-	-	-	-	+	-	-	-	-	-

Five *TIA1* mutation carriers underwent autopsy, four with clinical features of both ALS and FTD and one with ALS only. All had similar neuropathological findings characterized by chronic neurodegenerative changes and TDP-43 immunoreactive pathology that were anatomically widespread. Patients with FTD and ALS had preferential involvement of the prefrontal neocortex, substantia nigra, hypoglossal nucleus, and ventral grey matter of the spinal cord; whereas the patient with only ALS had more TDP-43 pathology in the motor cortex and less severe involvement of the non-motor neocortex. The morphological types of inclusions are illustrated in Figure S1. The severity, anatomical distribution and morphology of the TDP-43 pathology fit within the broad spectrum of what is typically encountered in other cases of familial and sporadic FTD/ALS. ALS, amyotrophic lateral sclerosis; CN XII, twelfth cranial nerve (hypoglossal) nucleus; CST, corticospinal tract; deg., non-specific changes of chronic

degeneration; FTD, frontotemporal dementia; GP, globus pallidus; n/a, not applicable; PAG, periaqueductal grey matter; SN, substantia nigra; TDP-43, TDP-43 immunoreactive pathology. Semiquantitative grading of pathology; -, none; +, mild; ++, moderate; +++, severe.